Molecular Cancer

RESEARCH Open Access

Integrating single cell- and spatial- resolved transcriptomics unravels the inter-tumor heterogeneity and immunosuppressive landscape in HBV- and *Clonorchis sinensis*-associated hepatocellular carcinoma

Jiayun Chen[2,3,1†], Wenmin Lu[1†], Yanni Lou[4†], Jing Liu[3†], Xiwen Liao[5†], Yunmeng Bai[2], Guangqing Cheng[2], Guangzhi Zhu[5], Ji Feng[1,6], Junqi Liu[5], Zhaoji Liu[7], Liqun Jia[4*], Jing Zhou[7*], Tao Peng[5*], Guo-Dong Lu[1,6*] and Jigang Wang[2,3,1*]

Abstract

Background Hepatocellular carcinoma (HCC) is the most common primary liver carcinoma with high lethality. Both of hepatitis B virus (HBV) and *Clonorchis sinensis* (*C. sinensis*) are critical infectious contributors to HCC development. However, the inter-tumor heterogeneity and tumor microenvironment (TME) of HCC patients with different infectious background remain largely unknown.

Methods We compiled a cohort of 269 primary HCC patients to assess the clinical impact of *C. sinensis* and HBV infections on patient prognosis. Single-cell RNA sequencing (scRNA-seq) and spatial transcriptomic (ST-seq) analyses were performed on tumor and adjacent normal samples from *C. sinensis*-associated HCC (CP), and double-infection HCC (DP) patients. Additionally, we integrated publicly available scRNA-seq and ST-seq datasets from HBV-associated (HP) patients. Immunofluorescence, immunohistochemistry and in vitro experiments were conducted to validate inter-tumor heterogeneity among the three HCC subtypes.

†Jiayun Chen, Wenmin Lu, Yanni Lou, Jing Liu and Xiwen Liao contributed equally to this work.

*Correspondence:
Liqun Jia
liqun-jia@hotmail.com
Jing Zhou
gardenia_zhou@hotmail.com
Tao Peng
p98720p@163.com
Guo-Dong Lu
lugd@fudan.edu.cn
Jigang Wang
jgwang@icmm.ac.cn

Full list of author information is available at the end of the article

Introduction

Primary liver cancer (PLC) is the third-highest cause of cancer-related mortality globally [1, 2]. Hepatocellular carcinoma (HCC) contributes to approximately 85% of PLC cases worldwide [3], with a 5-year relative survival rate of roughly 18% [4]. The main etiologies of HCC include chronic viral hepatitis, nonalcoholic fatty liver disease, and exposure to aflatoxin ingestions [5]. Hepatitis B virus (HBV), as a major risk factor of HCC, is capable of inducing a chronic and constant infection in host's hepatocytes and leading to severe liver dysfunctions [6]. Up to 423 million people worldwide suffer from chronic

Results *C. sinensis* infection is significantly associated with poorer prognosis in HCC patients. Multi-omics analyses revealed distinct inter-tumor heterogeneity in epithelial, immune, and stromal compartments across different HCC subtypes. Tumor cells in the DP group exhibited more malignant marker expression, higher copy number variation scores, increased activation of p53 pathway, and worse survival outcomes. Compared with other HCC subtypes, the TME in DP samples was enriched with *SPP1*$^+$ macrophages, exhausted CD8$^+$ T cells and *COL1A1*$^+$ fibroblasts. In contrast, the CP and HP groups showed higher proportions of M2-like macrophages and *ENPP2*$^+$ liver vascular endothelial cells, respectively.

Conclusion These findings decipher the cellular signatures and their interactions within the TME, shedding light on the inter-tumoral heterogeneity driven by different infections, and the development of targeted therapies for infectious HCC.

Keywords Hepatocellular carcinoma, Hepatitis B virus, *Clonorchis sinensis*, Single cell RNA sequencing, Spatial transcriptomics , Inter-tumoral heterogeneity

HBV infections and are at high risk of developing HCC, with the majority of cases occurring in Asia and Africa [7]. *Clonorchis sinensis* (*C. sinensis*), commonly known as the liver fluke, is a food-borne parasite predominantly found in China, Korea, northern Vietnam, and the Russian Far East [8]. It is estimated that around 15 million individuals worldwide are infected with *C. sinensis*, with China alone accounting for 13 million cases, particularly in Guangdong and Guangxi provinces [9]. In 2009, *C. sinensis* was classified as a Class I carcinogen of cholangiocarcinoma (CCA) by the International Agency for Research on Cancer (IARC) [10]. Moreover, recent research indicates that *C. sinensis* significantly influences the development of HCC [11–13], with infected patients facing a poorer prognosis than those uninfected [14].

The HCC tumor is characterized by a complex tumor microenvironment (TME), involving a variety of cellular components (tumor-infiltrating immune cells and stromal cells), chemokines, and the extracellular matrix [15]. The intricate interplay among these elements is pivotal for the tumor's occurrence, progression, and metastasis, and significantly impacts HCC patient survival and treatment outcomes [16, 17]. For instance, tumor immune barrier structures formed by the interaction of SPP1$^+$ macrophages and cancer-associated fibroblasts (CAFs) are linked to the immunotherapeutic efficacy [18]. In cases of recurrent HCC, an abundance of CD8$^+$ T cells with high KLRB1 expression is associated with a poor prognosis and tumor advancement [19]. A study by Chen *et al.* highlighted how the interaction between GDF15$^+$ cancer cells and dendritic cells suppress the presentation of tumor-associated antigens, impede T cell activation, and correlate with a poor prognosis in relapsed HBV-related HCC [20]. Tumor-associated neutrophils (TANs), particularly those enriched in the myeloid-cell-enriched subtype, are also associated with an unfavorable prognosis. The recruitment of macrophages by CCL4$^+$ TANs and the inhibition of T cell cytotoxicity by PD-L1$^+$ TANs are noteworthy mechanisms [21]. However, Current research on the impact of combined HBV and *C. sinensis* infections on HCC development, and how these pathogens reshape the HCC microenvironment are still unclear, whether in cellular or spatial dimension. Thus, further exploration of the TME characteristics and heterogeneity of HCC subtypes under single or double-infection conditions with these two pathogens, is of pivotal contribute to improving these patient classification, prognosis, and treatment.

Advancements in analytical technologies, such as single-cell RNA sequencing (scRNA-seq), have enabled the dissection of heterogeneous cellular states and the identification of transcriptional reprogramming in individual cell types [19, 22, 23]. And spatial transcriptomic sequencing (ST-seq) further allows for the measurement of gene expression patterns across different regions [24, 25]. The integration of spatial information has been instrumental in uncovering regional gene expression and intercellular communication networks uncovered by the scRNA-seq datasets. Prior studies have utilized these technologies to elucidate the composition of the HCC patient ecosystem and to dissect inter- and intra-tumoral transcriptomic heterogeneity, profiling the cellular states of various immunosuppressive immune and stromal cells during the development, metastasis, and treatment of primary HCC [18, 26]. However, there are few comparative analyses among different clinical HCC subtypes induced by distinct infection factors, such as HBV and *C. sinensis* [27, 28], limiting the comprehensive overview of the multi-faceted heterogeneity present in the infectious-associated HCC samples' TME at both the cellular and spatial levels.

In this study, we have integrated scRNA-seq with ST-seq methods to establish a multi-dimensional analysis, providing a comprehensive profile of cellular identities, TME landscapes, and intercellular interactions in HCC cases infected by HBV and *C. sinensis*. As depicted in Fig. 1A, our HCC cohort involved multiple clinical paired primary HCC samples and their adjacent liver tissues

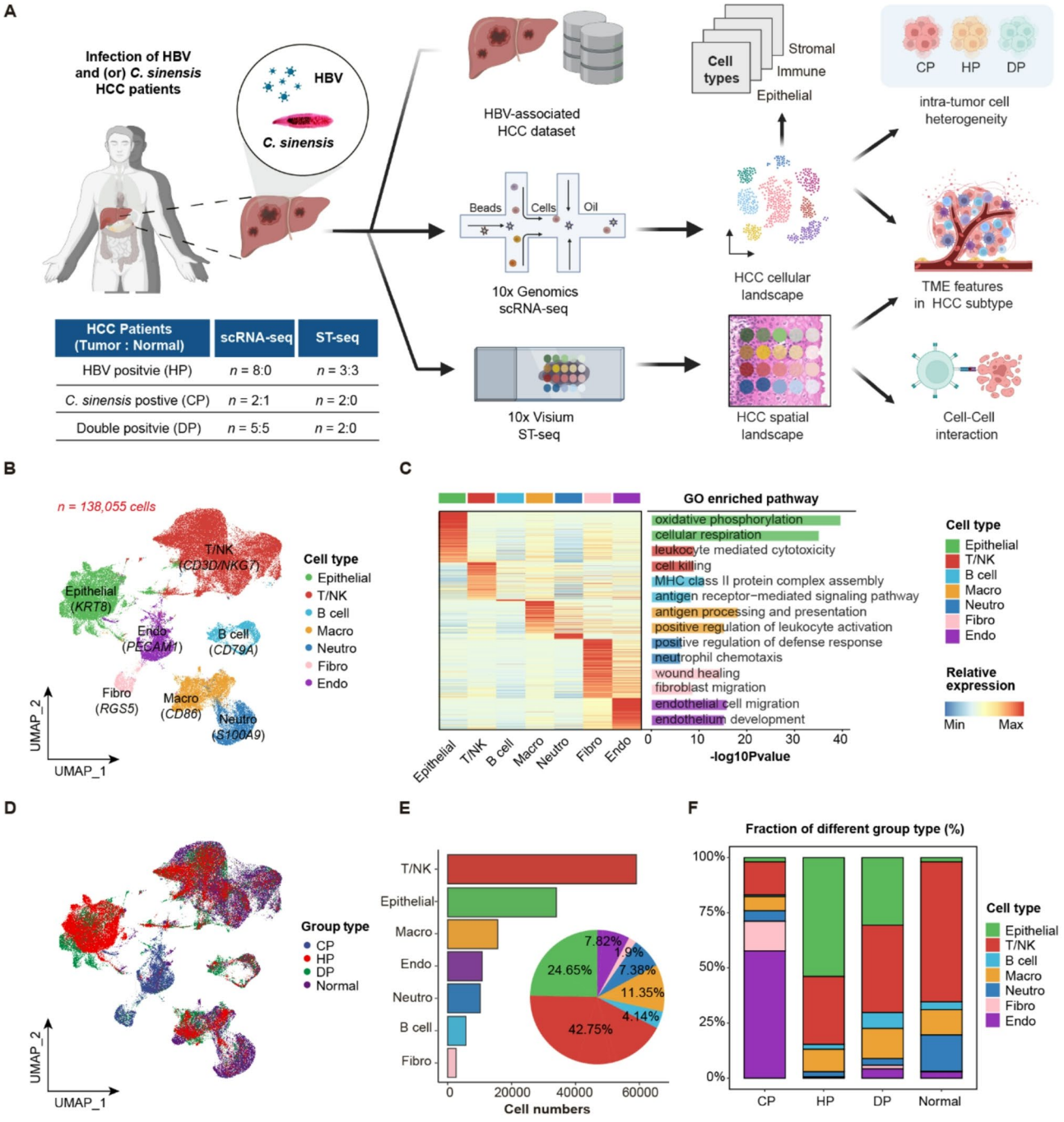

Fig. 1 Single-cell transcriptome landscape of HBV and *C. sinensis* - associated HCC cases. (**A**) Workflow of experiment design and HCC sample processing for scRNA-seq and ST-seq integrated analysis. (**B**) The UMAP visualization shows the clustering of 138,055 cells from all HCC samples in the scRNA-seq dataset. Clusters are labeled with cell types and markers, and colored by their inferred cell type. (**C**) The heatmap shows the expression patterns for marker genes across different cell types (left panel), and the barplot indicates the cellular-specific enriched biological pathway of each cell type (right panel) in the HCC datasets. The GO enriched terms were chosen with adjusted *P* value (corrected using the Benjamini-Hochberg procedure) < 0.05. (**D**) The UMAP plot shows the clustering of cells from all samples, colored by HCC subtypes (CP, HP, DP and Normal). (**E**) Bar plot shows the total cell number of each cell type, and the pie chart showing the proportion of the seven subpopulation cells in the scRNA-seq dataset. (**F**) Bar plot shows the percentage of identified various cell types across groups (CP, HP, DP and Normal)

from two patients infected solely with *C. sinensis* (CP) and five with double-infection of HBV and *C. sinensis* (DP). The demographic and pathological data of the seven randomly selected HCC cases are shown in **Table** S1. In detail, 13 samples from seven DP and CP patients underwent a robust scRNA-seq procedure using 10x Genomics Chromium platform, and four HCC samples were processed with ST-seq procedure using 10x Genomics Visium platform. Additionally, we incorporated 8 scRNA-seq datasets and 6 ST-seq datasets from HBV-associated (HP) primary HCC patients into our further analysis. Specifically, our objectives were to: (1) identify the representative cellular subtypes across epithelial, lymphocyte, myeloid and stromal cells; (2) characterize the altered pathways and their spatial features of TME in three HCC subtypes; and (3) investigate cell-cell interaction patterns within the TME at both cellular and spatial dimension. Our results systematically reveal the critical cellular subpopulation shaping inter-tumor heterogeneity of different HCC types, dissecting the inter-cellular interactions during HCC development, and provide novel insights int the design of efficacious therapies for infect-induced HCC patients.

Methods

Collection of information and samples of HCC patients

269 HCC patients of three primary HCC subtypes with prognosis information, were enrolled at the First Affiliated Hospital of Guangxi Medical University and underwent radical resection from April 2015 to June 2023. The clinical and follow-up information are summarized in Table S2. In this study, we used 13 tissue samples from seven HCC patients, with four samples analyzed for both scRNA-seq and ST-seq, and the other nine processed by scRNA-seq exclusively. The diagnosis of HCC was conducted strictly following the Guidelines for the Diagnosis and Treatment of Hepatocellular Carcinoma [29]. Two experienced pathologists confirmed the diagnosis through histology examination.

The inclusion and exclusion criteria for HCC patients were as follows: Inclusion criteria: (1) Patients who are undergoing radical surgery for primary treatment for the first time; (2) Patients with a confirmed pathological diagnosis of HCC; (3) Patients with complete baseline and follow-up data. Exclusion criteria: (1) Palliative surgery; (2) Perioperative mortality; (3) Intrahepatic cholangiocarcinoma, hilar/extrahepatic cholangiocarcinoma, metastatic liver cancer, combined HCC-ICC, tumors of undetermined origin, malignant tumors of other organs; (4) Recurrent HCC; (5) Underwent neoadjuvant therapy prior to surgery, such as chemotherapy, radiotherapy, local treatment, immunotherapy, targeted therapy; (6) The clinical and pathological data are incomplete. *C. sinensis* infection was defined with the presence of at least one of the following criteria: (1) A history of residence in endemic regions of *C. sinensis* and a record of consuming raw or undercooked freshwater fish or shrimp, accompanied by at least one of the following clinical findings: (a) Imaging studies revealing characteristic abnormalities; (b) A positive result from an enzyme-linked immunosorbent assay specific for *C. sinensis* antibodies. (2) Direct identification of adult worms or eggs of *C. sinensis* in the liver or gallbladder through intraoperative or postoperative pathological examination. (3) Detection of *C. sinensis* eggs in stool samples via microscopic evaluation [30]. HBV infection was confirmed by the presence of hepatitis B surface antigen in the patient's preoperative serum (qualitative) [31].

Single-cell suspension Preparation

Fresh tumor and healthy liver tissues were cut into 1–2 mm^3 pieces with scissors and digested in a solution containing 3 mg/ml of collagenase II (Sigma, C2-28-100MG), 0.5 mg/ml of hyaluronidase (Sigma, H1115000), and 0.02 mg/ml of DNA enzyme I (Sigma, DN25-100MG) for 30 min at 37 °C. The enzymatic reaction was then stopped by adding 10 ml of DMEM/F12 complete medium. The digested mixture was filtered through a 70 μm cell filter, and the filtered suspension was centrifuged at 4 °C, 50 g for 2 min. The supernatant was discarded, and 1 ml of pre-cooled 1× Red Blood Cell Removal Solution was added to resuspend the cells by gently mixing. The cells were then incubated at 4 °C for 10 min. After incubation, 10 ml of pre-cooled Wash Buffer was added to the cells, followed by incubation for 2 min at 4 °C, 300 (Relative Centrifugal Force, RCF). The supernatant was then removed by blotting. The cells were incubated again at 4 °C for 10 min, followed by the addition of 10 ml of pre-cooled Wash Buffer and centrifugation at 4 °C for 10 min at 300 RCF. The supernatant was pipetted up, and 5 ml of pre-cooled Wash Buffer was added. The cells were gently mixed.

Singlet cell capture, library construction, and sequencing

Take an appropriate amount of single cell suspension and mix it with 0.4% Taipan Blue Stain Solution at a ratio of 9:1, then use Countess® II Automated Cell Counter to count the cells and calculate the percentage of viable cells. Ensure that the percentage of viable cells is ≥ 90% and that the cell concentration is set to the desired concentration (not less than 1000 cells/μL). Firstly, cDNA was digested and broken into fragments of about 200 ~ 300 bp, and then PCR amplification was carried out to obtain the DNA library after the library construction process of traditional second-generation sequencing, such as sequencing connector P5 and sequencing primer R1. Each cell was subjected to 3' sequencing using Single-Cell 3'Library and Gel Bead kit V2 (10x

Genomics, Pleasanton, USA) following the manufacturer's instructions.

Sample Preparation for spatial transcriptomics analysis

Tissues were snap-frozen and embedded with OCT embedding agent. At low temperature, a 10-μm-thick slice was cut from the tissue block and attached to the Tissue Optimization Microarray and Library Preparation Microarray, respectively, using the frozen section technique. The sections were then fixed with pre-cooled methanol and stained with hematoxylin-eosin (H&E) stain. Tissue staining results were obtained by bright-field microscope to record the tissue morphology and spot position.

Spatial transcriptome library Preparation and sequencing

Use the library preparation chip to prepare spatial transcriptome libraries. The microarray with bright field imaging was permeabilized according to the optimal tissue permeabilization time (18 min), and the tissue mRNA was released to bind with the captured sequence on the microarray, reverse transcription to synthesize cDNA fragments and mark the spatial position, and PCR amplification to synthesize the cDNA biallelic. By denaturing the cDNA in alkaline environment, the cDNA duplex will be released into liquid free environment, and the cDNA duplex will be used as a template to further amplify and synthesize a large amount of cDNA. cDNA will be enzymatically interrupted into a 200–300 bp fragment, and then P5 connector, i5 sample index, read 2, i7 sample index and P7 connector will be used to construct a standard sequencing library. High-throughput sequencing was performed on the constructed library using the dual-end sequencing mode of the Illumina sequencing platform.

H&E staining

HCC tumor tissue samples were fixed in 4% paraformaldehyde for 24 h and then embedded in paraffin. A rotary microtome sliced the paraffin blocks into 4 μm thick tissue sections. The sections were dewaxed in xylene twice for 5–10 min each. The sections were gradually rehydrated with serial ethanol concentrations of 100%, 95%, 85%, 75%, and 0% for 3 min each. Sections were stained with hematoxylin staining solution for 2 min, washed with distilled water to remove excess dye, differentiated in differentiation solution for 3 min, and rinsed twice with tap water for 2 min each time. The sections were placed in eosin staining solution for 1 min, washed with distilled water for 3 s, and dehydrated quickly. Tissue dehydration and transparency were achieved by immersing the samples in 75%, 85%, 95%, and 100% ethanol for 2–3 s each, followed by 100% ethanol for 1 min and clearing in xylene twice for 1 min each. Finally, the samples were sealed with neutral gum sealed. The sections were observed under a microscope.

Immunofluorescence (IF) staining

Histological evaluation of hepatocellular carcinoma samples was performed by fixing, dehydrating in sucrose, and embedding in OCT. Immunofluorescence staining was carried out for each sample. The tissue sections were baked, fixed, and closed using microwave-induced antigen repair with EDTA solution (ZSGB-BIO, ZLI-9079). Primary antibodies including N-cadherin (Proteintech, 22018-1-AP), Vimentin (Proteintech, 10366-1-AP), p21 (Proteintech, 10355-1-AP), p53 (Servicebio, GB12626-100), CD68 (Servicebio, GB113150), MRC1 (Servicebio, GB115273), SPP1 (NOVUS, NB110-89062SS), CD8A (Servicebio, GB12068), PDCD1 (Abcam, ab52587), CD4 (Abcam, ab288724) and FOXP3 (Servicebio, GB112325) were used. After incubation with secondary antibodies (HRP-anti-rabbit IgG, Alexa Fluor 488 Labeled Goat Anti-Rabbit IgG, Alexa Fluor 488 Labeled Goat Anti-Mouse IgG, or HRP-anti-mouse IgG), the cell nuclei were stained with DAPI and anti-fluorescence attenuating reagent was added. Images were scanned using Nikon Eclipse C1 or ZEISS Axio Imager M2p.

Immunohistochemical staining (IHC)

For tissue sections, they were baked, fixed, and antigenic repair was performed using EDTA. Immunohistochemistry was carried out using the Universal two-step Test Kit (Mouse/Rabbit Enhanced Polymer test system) (ZSGB-BIO, PV9000). Briefly, sections were incubated with a 1:100 dilution of HepPar-1 (ZSGB-BIO, ZM-0131), ARG-1 (Proteintech, 16001-1-AP), GPC-3 (Proteintech, 30021-1-AP), NOTCH4 (Signalway Antibody, 37195), COL1A1 (Bioss, bs-10423R) or ENPP2 (Signalway Antibody, 42644) overnight at 4 °C, followed by incubation with goat anti-rabbit for 20 min at room temperature. Sections were incubated with DAB (ZSGB-BIO, ZLI9018) for 6–8 min, re-stained with hematoxylin, dehydrated and mounted. Images were scanned with EVOS FL Auto Imaging System.

scRNA-seq data processing

We subjected the raw scRNA-seq data from HCC cases to demultiplexing, alignment against the GRCh38 (reference genome; Download from10x Genomics website) and counting using Cell Ranger toolkit (version 6.0.1) provided by 10x Genomics. We quantified the number of unique molecular identifiers (UMIs) and genes for each cell. The resulting gene-cell matrix underwent further quality control and preprocessing using Seurat package (version 4.0.5) [32], with default parameters unless otherwise stated. We performed data filtration to eliminate low-quality cells that expressed fewer than 200 genes or

had more than 500 unique molecular identifiers (UMIs). Cells with a mitochondrial proportion within the range of less than 20% were excluded (Table S3). The remaining data were normalized and scaled using the *SCTransform* function and subjected to principal component analysis (PCA) using the *RunPCA* function on the matrix for evaluating the embedding were the similarity as those used for clustering. The Harmony algorithm (version 0.1.0) [33] was employed to minimize the potential batch effects on the gene-cell-barcode count matrices and facilitate unsupervised embedding for the multiple single-cell datasets. For visualization, we utilized the uniform manifold approximation and projection (UMAP) algorithm with Seurat's *RunUMAP* function for non-linear dimensionality reduction (ratio = 0.8) of each dataset, arranging single cells in a two-dimensional space. We used various cell-type-specific makers and the unsupervised clustering results generated by the *FindClusters* function for cell identification.

Spatial transcriptomics data processing

Using the 10x Genomics Loupe Browser (version 6.0.0) software, we first manually removed the spots associated with defected or incomplete tissues in the slides to generate the corresponding position corrected file (.json) for each slide in the subsequent analysis. In addition, we integrated 6 public ST-seq datasets of HCC tumor tissue as HP group for further analysis [24]. The Space Ranger (version 1.0.0) package was used to process the raw sequencing data. For each slide, the raw gene-spot matrices were imported into a Seurat object. Genes expressed in less than 3 spots were filtered out for subsequent analysis. After filtering, ST datasets were merged and variance-stabilized using *SCTransform* function with 3000 variable features. PCA was performed to reduce dimensionality of data using *RunPCA* function, retaining the top 40 components based on the inspection of the *ElbowPlot* function. Clustering was performed using the SNN algorithm using *FindNeighbors* and *FindClusters* functions (resolution = 0.8) and visualized UMAP using *RunTUMAP* function. For spots type annotation, we applied the *AddModuleScore* function, we evaluated spots' module scores based on the cellular marker genes listed in the previous report [34] and scRNA-seq dataset.

Multimodal intersection analysis (MIA)

MIA package [35] infers the enrichment of identifiable cell types in a targeted tissue region by conducting a hypergeometric test to assess the extent of overlap between spatial region-mapped genes and cell-type-specific genes identified by single-cell data. Based on the cell type and gene expression information of the single cell dataset, we applied the MIA package to use the test values to assess the enrichment level of various cell types in the ST-seq dataset.

Identification of differential expression genes

The Seurat's *FindAllMarkers* function was used to detected markers for each cluster with the parameters: log-scaled change = 0.25; min.pt = 0.25, only.pos = TRUE. We conducted differential expression analysis between two groups using the Seurat's *FindMarkers* function to identify the DEGs (Wilcoxon Rank-Sum test; the threshold: |log-scaled fold change| > 0.25, adjusted *P* value < 0.05). The marker genes or DEGs per group were enriched for Gene Ontology (GO) function using the *clusterProfiler* toolkit (version 4.0.2) in R [36].

Gene set variation analysis (GSVA)

To explore the pathway activities of tumor cells and cluster spots, GSVA package (version 1.38.2) [37] was implemented to quantify the signature activities of 50 hallmark pathways from MSigDB database [38]. Furthermore, differential pathways between groups were identified using the *limma* package (version 3.46.0), with statistical significance defined by an adjusted *P*-value < 0.05.

Inference of copy number variations from single-cell data

We subject the gene-cell count matrix from the integrated Seurat Objects as input to InferCNV package (version 1.12.0) [39, 40]. We applied inferCNV's *CreateInfercnvObject* function with the recommended cutoff value of 0.1, to infer the CNV profiles across each chromosome of the tumor cells in comparison to control cells. For normal cells, we sampled both immune cells and stromal cells as the reference. All tumor epithelial cells were input as inquiry group. Other settings were set as defaults.

$CD8^+$ T exhausted cells' state inference through trajectory analysis

To detect the cell status of the lymphocyte in the HCC TME, we conducted the pseudotime analysis using the Monocle 2 package [41] that describe multiple fate decisions within an unsupervised manner to infer the cell differentiation trajectory of $CD8^+$ T exhausted cells. We created a *CellDataSet* object with the default parameter. After dimension reduction and cell ordering, the cell trajectory was reconstructed as the cell progresses through the differences in heterogeneity across groups under study. We performed the branched expression analysis modeling (BEAM) using the *BEAM* function to analyze the branch point as well as cluster the results, with GO analysis subsequently applied to each cluster. The trajectory was visualized by each group and pseudotime using *plot_genes_branceed_heatmap* function.

Cell functional scores definition

The Seurat's *AddModuleScore* function on R tool was utilized to calculate functional scores for describing the functional characterizes of each cell cluster. For epithelial cells, liver cancer stem cell-related genes were defined as in [27]. As for T cells, regulation-related and exhaustion-related genes were previously described in [42]. For macrophages, the genes for pro-inflammation score and anti-inflammation score were extracted from our predefined sets, including *Tnf*, *Cd163*, *Mrc1*, *Cd68*, *Il1b*, *Il10*.

Cellular communications

We employed CellChat R package (version 1.4.0) [43] to detect significant ligand-receptor (L-R) pairs within HCC cases of each origin. The expression matrix and target cell subtypes for Normal, CP, HP and DP groups were initially input into CellChat, and merged into an integrated object via *mergeCellChat* function, then the differential number of interactions between tumor and normal groups were calculated by *netVisual_diffInteraction* function. We identified the differentially expressed pathways of CP *versus* (vs.) Normal, HP vs. Normal and DP vs. Normal groups by *rankNet* function, and visualized the intercellular connections using *netVisual_bubble* function. Besides, the significance scores of key L-R pairs in spatical location were visualized by *lr_result_plot* function using stLearn toolkit (version 0.4.0).

Survival analysis

RNA-seq from The Cancer Genome Atlas (TCGA) and clinical cases of liver hepatocellular carcinoma (LIHC) were used to evaluate the prognostic effects of gene sets derived from specific cell states. Briefly, DEGs among Normal, CP, HP and DP epithelial cells were used to calculate GSVA scores, then divided into high/low groups based on score's quartile. The survival curves were compared using log-rank tests by *survfit* function of survival package (version 3.5-3). Besides, we applied *coxph* function to calculate hazard ratio (HR) of macrophages based on cluster-specific DEGs' scores, and visualized via *ggforest* function.

Cell culture

The human HCC cell lines HepG2 and HepG2.2.15, and the human monocyte cell line THP-1, were obtained from authenticated cell culture repositories. HepG2.2.15, which carries the complete HBV genome and stably expresses and replicates HBV in culture, and the HepG2 cell line were cultured in Dulbecco's Modified Eagle's Medium (DMEM) supplemented with 10% fetal bovine serum (FBS) and 1% penicillin-streptomycin. G418 (500 μg/mL) was added to the HepG2.2.15 culture for selection.THP-1 cells were cultured in RPMI-1640 medium (Gibco) supplemented with 0.5 mM β-mercaptoethanol (Merck, M6250), 10% FBS, and 1% penicillin-streptomycin to maintain exponential growth. To generate macrophages, THP-1 cells were seeded in 6-well plates and treated with 200 nM PMA (MCE, HY-18739) for 48 h to induce differentiation into macrophages. For the macrophage-HCC cell co-culture, a conditioned medium-based approach was employed. Briefly, the culture medium from HepG2 and HepG2.2.15 cells (either treated or untreated with CsESPs) was collected, centrifuged at 3000 rpm for 10 min, and the supernatant was filtered through a 0.22 μm sterile filter to obtain the conditioned medium. The macrophages were then cultured in this conditioned medium for 48 h.

Preparation CsESPs

The second intermediate host of *C. sinensis*, *Pseudorasbora parva*, was obtained from Hengzhou, Guangxi, where natural metacercarial infection was confirmed. To isolate the parasites, fish tissues were enzymatically digested using a simulated gastric fluid containing 0.5% pepsin, 1% HCl, and 0.9% NaCl, incubated at 37 °C for 12 h. Adult male Sprague-Dawley rats, supplied by the Laboratory Animal Center of Guangxi Medical University, were housed under conditions adhering to NIH guidelines for ethical animal use (Approval No. 202410011). Each rodent received an oral inoculation of 150 metacercariae, which were manually isolated under microscopic guidance.

After an 8-week infection period, the animals were humanely sacrificed under anesthesia. Adult flukes were then harvested from the biliary tracts and incubated in PBS at 37 °C with 5% CO_2 supplementation. Following a 6-hour incubation period, the culture supernatant was centrifuged at 12,000 g (4 °C, 10 min) to obtain *C. sinensis* excretory-secretory products (CsESPs). The supernatant was filtered through a 0.22 μm membrane and cryopreserved at -80 °C. Protein quantification was performed using the BCA method.

quantitative polymerase chain reaction (qPCR)

Total RNA was isolated using TRIzol reagent following the standard protocol recommended by the manufacturer. For quantitative analysis of gene expression, qPCR was carried out with 2× Universal Blue SYBR Green qPCR Master Mix (Servicebio) according to the established procedures. The housekeeping gene GAPDH was used as an endogenous reference to normalize the data. All oligonucleotide primers employed in this study were commercially synthesized by Sangon Biotechnology Ltd., with their exact nucleotide sequences provided in Table S4.

Statistical analysis

We performed statistical analysis using the software in R package and GraphPad Prism (version 8). Data are presented as mean ± SEM as stated from at least three independent experiments. To assess intergroup differences, either Student's t-test (for normally distributed data) or the Mann-Whitney U test (for non-parametric distributions) was applied. For multi-group comparisons, one-way ANOVA was performed, supplemented by post hoc analyses (LSD test or Games-Howell adjustment, as appropriate). P value < 0.05 indicates a statistically significant.

Results

CP and DP patients exhibit poorer prognosis in the HCC cohort

To assess the clinical implications of *C. sinensis* infection on the prognosis of HCC patients, we compiled a cohort of 269 primary HCC patients underwent radical surgery with available prognostic information. There were 33 cases in CP, 129 cases in HP, 90 cases in DP, and 17 cases in double-negative for both *C. sinensis* and HBV. In the case of primary HCC patients, the median overall survival (OS) was 79.4 months in HBV-negative *vs.* 80.67 months in HBV-positive ($P = 0.7648$), the median OS was 73.38 months in *C. sinensis*- positive *vs.* 85.17 months in *C. sinensis*-negative ($P = 0.0014$), the OS was 75.11 months in CP *vs.* 84.54 months in HP *vs.* 68.32 months in DP ($P = 0.0189$) (Fig. S1 A-C). These results indicated that *C. sinensis* infection is significantly linked with HCC patients' poorer prognosis, with those having double-infection (DP) faring worse than those with single infections (CP and HP).

To determine whether *C. sinensis* could serve as an independent prognostic predictor of OS, we performed a univariate Cox regression analysis. As shown in Fig. S1 D, with HP as reference, *C. sinensis* was found to be significantly associated with OS [Hazard ratio (HR) = 2.97, 95% (Confidence Interval, CI) = 1.331–6.60, $P = 0.0078$]. Subsequently, *C. sinensis*, along with age, sex, and Barcelona Clinic Liver Cancer (BCLC) stage, were included in a multivariate Cox regression analysis. This analysis confirmed that *C. sinensis* still serve as an independent prognostic predictor after adjusting for other confounding factors (HR = 2.782, 95% CI = 1.211–6.39, $P = 0.0159$, Fig. S1 E).

Single-cell transcriptomic profiling of CP, HP, and DP-infected HCC patients

Here, we obtained and integrated the scRNA-seq datasets from all 21 samples (including 8 HP, 2 CP, 5 DP, and 6 Normal, respectively), and obtained a total of high-quality 138,055 cells with stringent quality control (Fig. S2 A, Table S3). We integrated these cells into a normalized and un-batched dataset and further subjected them to PCA for dimensional reduction, which resulted in 33 distinctive clusters as visualized in UMAP (Fig. S2 B). According to the expression levels of canonical marker genes [27], those cells were annotated into seven major cell types, including epithelial cells (Epithelial, *KRT8*$^+$), T cells and natural killer cells (T/NK, *CD3D*$^+$*NKG7*$^+$), B cells (*CD79A*$^+$); macrophages (Macro, *CD86*$^+$) and neutrophils (Neutro, *S100A9*$^+$); endothelial cells (Endo, *PECAM1*$^+$) and fibroblast (Fibro, *RGS5*$^+$) (Fig. 1B, Fig. S2 C).

Moreover, we identified the significantly differentially expressed genes (DEGs) for each cell type (P_val_adj < 0.05, and avg_$\log_2$FC ≥ 0.25) and subjected them to Gene Ontology (GO) enrichment analysis. The representative cellular biological processes highly correlated with the cell identities, such as oxidative phosphorylation in Epithelial, leukocyte mediated cytotoxicity in T/NK (Fig. 1C). Interestingly, we found extensive intratumoral heterogeneity, as shown by the mixed representation of intra- and inter-patient cells by UMAP (Fig. 1D, Fig. S2D). Both of carcinoma and non-carcinoma cells might contribute to the observed HCC intratumoral heterogeneity, which is similar with the observation in breast cancer and lung cancer [44, 45].

Among these cell types, we observed that the dataset predominantly consisted of T/NK ($n = 59{,}024$, 42.75%) and Epithelial ($n = 34{,}033$, 24.65%) (Fig. 1E). This result also revealed that the tumor-derived Epithelial, Macro and stromal cells (Endo and Fibro) have relatively higher proportions in comparison to Normal group (Fig. 1F). We also observed distinct prevailing cell types for each group, such as Epithelial in HP, and T/NK in DP group (Fig. S2E).

Spatial transcriptomic landscape of CP, HP, and DP-infected HCC samples

We concurrently conducted ST-seq analysis using the 10x Genomics Visium platform for the fresh HCC tissues from both the CP and DP cohorts. Additionally, we also incorporated 3 Normal and 3 HP-derived samples from public Visium datasets for further comparative analysis at spatial dimension (Fig. 1A) [24]. Collectively, we obtained spatial transcriptomes across 32,072 spots from 10 slides (Fig. S3A). The spots' number ranges from 1,061 in the T0422 to 4,733 in the HCC_2T sample (Fig. S3B). These dataset were integrated into a normalized, un-batched dataset comprising 14 distinct spot clusters (C0 to C13) that spanned various group types and samples (Fig. 2A-B, Fig. S3C). To profile the spatial transcriptomic alteration of various cell types identified in the scRNA-seq dataset, we assigned main spots' identities such as Epithelial, Endo, and Macro to the spots in our consolidated ST-seq dataset. However, given the limited resolution of Visium

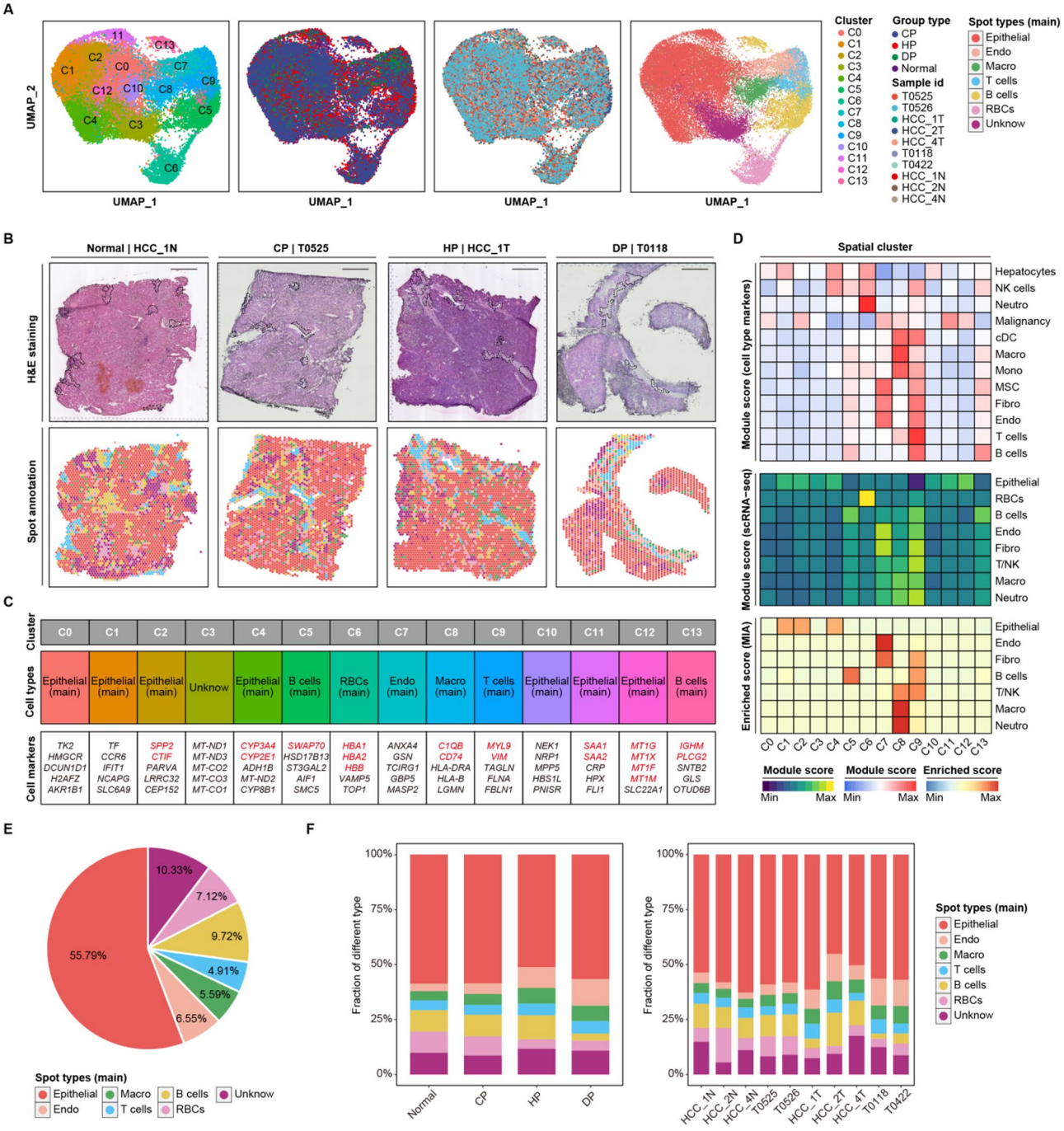

Fig. 2 Spatial transcriptome atlas of CP, HP, and DP-infected HCC samples. (**A**) The UMAP plots show the unsupervised clustering of ST spots, grouped by clustering id, group types, samples id, and assigned spot types, respectively. (**B**) The H&E staining (top panel) and the corresponding spatial annotation of spot types (bottom panel) of HCC_1N (Normal group), Normal T0525 (CP group), HCC_1T (HP group), and T0118 (DP group), scale bar = 1 mm. (**C**) Marker genes of each cluster of the main spot types. Some marker genes are of specific cell types were highlight in red. (**D**) The heatmap show the module score of cell types based on classical cell type markers (top panel) and cellular module of cell types (middle panel), and MIA enriched scores (bottom panel) across each spatial cluster in the ST-seq dataset. (**E**) The pie charts show the spot numbers and relative proportion of various spot types in the ST-seq dataset. (**F**) The bar plots show the relative proportion of spot types among various groups (left panel) and samples (right panel) in the ST-seq dataset

(55 μm/spot), some regions of the HCC sample such as the immune cell infiltrating region might encompass numerous cells and various cell types. Thus, we employed multiple approaches to evaluate the accuracy and gain a more nuanced understanding of spot identities.

Firstly, we performed DEGs analysis for each cluster (P_val_adj < 0.05 and avg_$\log_2$FC ≥ 0.25), revealing that the main cellular type exhibited a high specificity of cellular marker expression pattern (Fig. 2C). For instance, elevated expression level of *C1QB* and *CD74* in the cluster8 (assigned as Macro), and *SAA1* and *SAA2* in the cluster11 (assigned as Epithelial). Secondly, we evaluated cellular module scores of spots within the ST-seq dataset, leveraging the cellular DEGs profiled in our scRNA-seq dataset (Fig. 1C) and cellular marker list reported in Ho *et al.*'s study [27]. To further explore the cellular composition of various spot types, we also performed MIA method to the ST-seq dataset [35]. Both of cellular module and MIA scores of various cellular labels could be mapped concordantly to the spots' identities (Fig. 2D). For instance, we observed Macro (main), and Epithelial (main) spots have high specificity of the corresponding cellular types in the enrichment results. This high degree of consistency across various annotation methods, underscores the reliability of our spot identity assignments, despite the lack of single-cell resolution with Visium.

In total, we compiled a pre-annotated ST-seq dataset including seven main spot types: Epithelial (55.79%), Endo (6.55%), Macro (5.59%), T cells (4.91%), B cells (9.72%), RBCs (7.12%), and Unknow (10.33%) (Fig. 2E). We further assessed the spot proportion of each sample and found a similar proportional distribution among the different groups and samples (Fig. 2F). This comprehensive dataset lays the foundation for a deeper investigation into the spatial divergence of cellular distribution and the activity of enriched pathways.

Dissecting inter-heterogeneity of epithelial cell across diverse HCC groups

We proceeded to dissect the heterogeneity of the Epithelial within HCC by conducting a multimodal investigation. An unsupervised re-clustering analysis was applied to compare the epithelial profiles across various sample and group types. HCC tumor-epithelial cells mainly aggregated based on their group type and sample origin, with only a scattering of Normal-derived cells evident in our analysis, underscoring the pronounced inter- and intra-group heterogeneity (Fig. 3A). The cellular number of Epithelial ranges from 257 in the CP group to 19,293 in the HP group, reflecting the diverse composition within each group (Fig. S4A). We also observed higher correlation coefficients in the expression patterns of the Epithelial among the three HCC subtypes compared to the Normal group (Fig. S4B).

Utilizing HCC-associated markers, we characterized distinct expression patterns in HCC epithelial cells, particularly in the DP group. α-fetoprotein (AFP) [46], Glypican-3 (GPC3) [47], and arginase-1 (ARG-1) genes were elevated in the DP-derived Epithelial, while Hepatocyte Paraffin 1(Hep par-1/carbamoyl phosphate synthetase I, CPS1) in Epithelial of CP group were expressed higher level than other subtypes (Fig. 3B). These marker expression patterns were further validated by IHC analysis (Fig. S4C).

To further explore the genomic heterogeneity of Epithelial from the three HCC groups relative to the Normal group, the alterations of chromosomal-scale CNV among the Epithelial were assessed via InferCNV method [39, 40]. Similar CNV patterns, such as duplications in chromosomes 1+, 7+, and 19+, were observed. Notably, DP-derived Epithelial displayed distinct chromosomal variations, including duplications in chromosomes 9+, 10+, and 22+, with significantly elevated CNV scores compared to other groups (Fig. 3C, Fig. S4D). Moreover, we evaluated the liver hepatocellular carcinoma (LIHC) and immune surveillance scores of Epithelial across 4 group types, finding that HCC Epithelial (especially in HP and DP) exhibited higher LIHC and lower immune surveillance scores than the Normal group (Fig. S4E-F). Notably, survival analysis revealed that patients in the DP group had significantly poorer overall survival compared to the other two HCC groups ($P = 0.045$) in the LIHC cohort of TCGA dataset (Fig. 3D, Fig. S4G).

To uncover the transcriptomic shifts of Epithelial across different group types, we subsequently conducted DEGs analysis for each different group type (P_val_adj < 0.05 and avg_$\log_2$FC ≥ 0.25), followed by GO enrichment analysis. As for the GO enriched pathways, pathways such as epithelial cell migration and endothelial cell migration were up-regulated in the CP-derived Epithelial, oxidative phosphorylation and electron transport chain in the HP-derived Epithelial, as well as viral gene expression and protein localization to endoplasmic reticulum in the DP-derived Epithelial. These results highlight the heterogeneity of three HCC group types in biological processes' activity (Fig. S4H-J).

Furthermore, using human hallmark gene sets, we performed GSVA upon Epithelial of four groups and determined the group-type specific up-regulated pathways via Limma (P_val_adj < 0.05 and $\log_2$FC ≥ 0), and evaluated the concordance of up-regulated and/or down-regulated hallmark pathways from three HCC groups compared with the Normal group (Fig. 3E). There were several metabolic pathways such as bile acid metabolism and fatty acid metabolism commonly up-regulated between HP and DP groups, and the up-regulation of epithelial mesenchymal transition (EMT) between CP and HP groups. Notably, we identified that Epithelial from the DP group

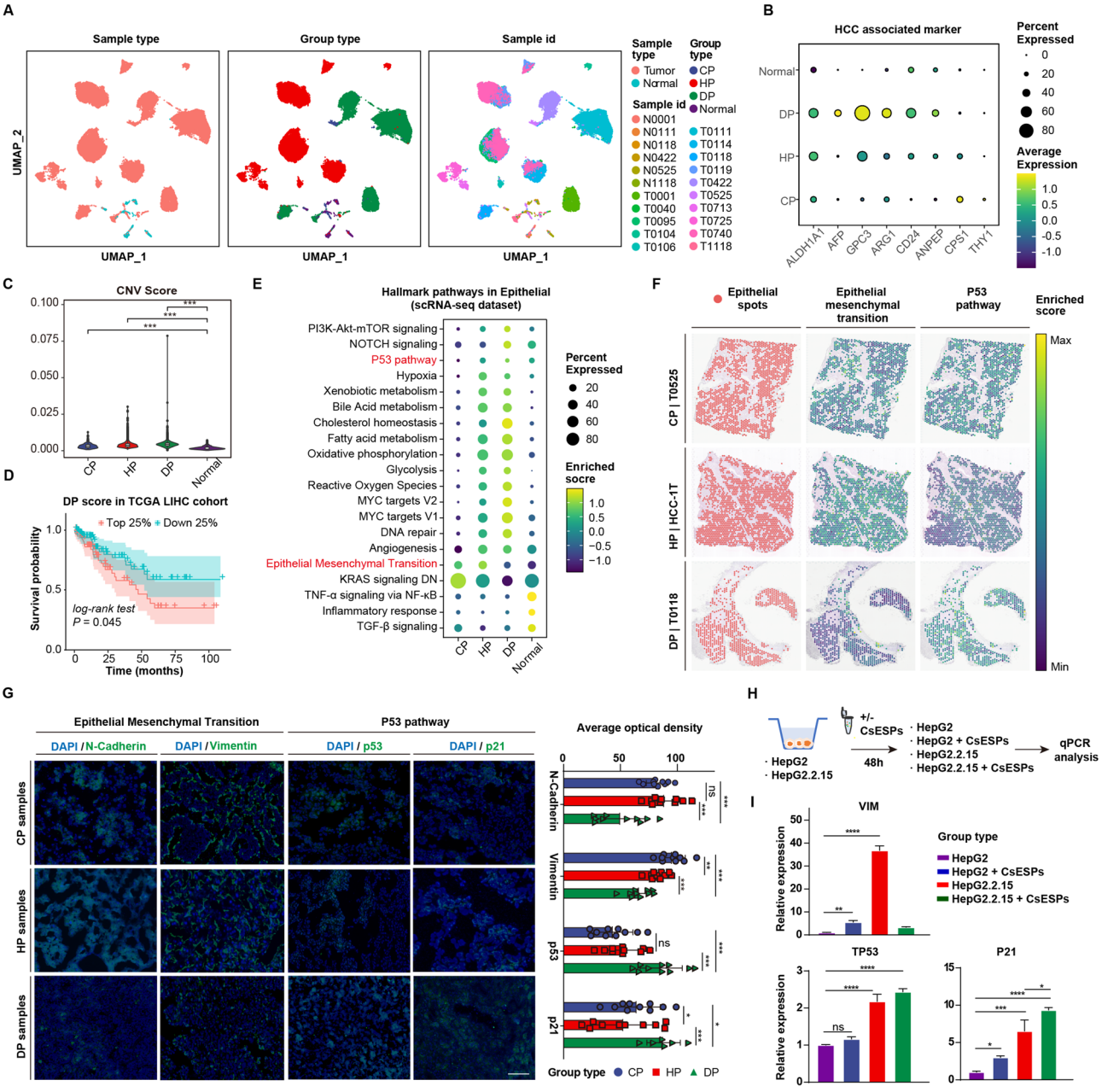

Fig. 3 Figure 3I: The label "Tp53" has been corrected to "TP53".The label "p21" has been corrected to "P21".

up-regulated pathways including p53 pathway, NOTCH signaling, and hypoxia, which indicates that DP group-derived Epithelial might harbor higher malignancy compared with other HCC group types. On the contrary, we noticed that the down-regulated immune response-associated pathways such as TNF-α signaling via NF-κB and inflammatory response among three groups compared with the Normal group, indicating the inhibitory immune response of Epithelial from HCC groups.

In parallel, we subset the Epithelial spots from our ST-seq dataset and evaluated the module scores of EMT and p53 pathway. We found that the activation of EMT pathway in the CP and HP samples, andp53 pathway in the DP samples (Fig. 3F). Moreover, IF staining demonstrated that epithelial cells were co-localize with N-Cadherin and Vimentin protein expressions in the CP and HP samples, with higher expression level than that in the DP group. By contrast, we found the elevated expression level of p53 and p21 in the DP group than other two HCC subtypes (Fig. 3G).

To further validate the pathway activity of Epithelial, we conducted an in vitro experiment to investigate the double-infection effects of *C. sinensis* and HBV upon activation in malignant cells (HepG2 and HepG2.2.15).

Specifically, we detected the activation of EMT and p53 signaling pathways in malignant cells following treatment with 100 μg/ml of CsESPs, as assessed by qPCR. Our findings demonstrated significant up-regulation of VIM (encoding Vimentin) expression in both CP and HP groups. Notably, increased expression levels of TP53 (encoding p53) and P21 (encoding p21) were observed specifically in the DP group (Fig. 3H-I). Collectively, these results indicate the heterogeneity of Epithelial across different HCC subtypes at HCC-related marker pattern, genomic alteration, survival state, and activated pathways.

Revealing the tumor-associated macrophage cells across different HCC groups

Previous studies have also expanded our understanding of the crucial role of myeloid cell during HCC occurrence, development, and metastasis [19, 23]. In our single-cell dataset, we performed re-clustering analysis on myeloid cells and identified a total of 16 cell subgroups with unique expression signatures, including seven Macro subgroups (termed as Macro1-7: *SPP1*$^+$ Macro, *DAB2*$^+$ Macro, *TREM2* + Macro, *CD163*$^+$ Macro, *CXCL9*$^+$ Macro, *MT1G*$^+$ Macro, and *APOH*$^+$ Macro), three Neutro subgroups (Neutro1-3), three from dendritic cells (DC1-3) with elevated *CLEC9A*, *CLEC10A* and *LAMP3* expression, one proliferative cells (Cycling) with high *MKI67* expression, and two monocytes (Mono1-2) (Fig. 4A-B). As for Macro subtypes, we observed that Macro1, Macro2, and Macro3 were characterized with high expressions in *SPP1*, *DAB2*, and *TREM2* expression, respectively. Next, we found that Macro2 with a M2-like signature (*CD163*$^+$*MRC1*$^+$) were primarily observed in the CP group, Macro3 with higher *TREM2* expression in the HP group. Interestingly, Macro1 with *SPP1* expression, which have been reported as the tumor-associated macrophages (TAMs) in driving tumor development, were predominant in the DP group. Cellular proportion analysis underscore the complexity of myeloid immune landscape within HCC cases (Fig. 4C).

Notably, Macro1 from the DP group uniquely exhibited the elevated expression of genes *SPP1* and *IL1B*, suggesting that *SPP1*$^+$ macrophages serve as a crucial cell population in shaping TME features of DP (Fig. 4D). Furthermore, we performed hazard analysis to evaluate the clinical relevance of three Macro subgroups (Macro1, 2 and 3) in the TCGA LIHC cohort ($n = 374$). We found that *SPP1*$^+$ Macro1 was associated with a significantly higher hazard ratio (HR = 3.087, $P = 0.0271$) compared to the other subgroups, indicating that the higher score of Macro1 subgroup associated with the poorer prognosis in HCC patients (Fig. 4E).

To evaluate the spatial distribution of three Macro subgroups across different subgroups, we performed DEGs analysis to generate module gene list for each subgroup from the scRNA-seq dataset, than we evaluate the module score of these three Macro subgroups across different HCC samples in the ST-seq dataset. In agreement with the enrichment results in the scRNA-seq dataset, we found that DP sample exhibited the distribution of Macro1 subgroup with elevated enrichment scores, while samples in CP and HP showed increased Macro2 and Macro3 signature scores and spatial distribution, respectively (Fig. 4F). Furthermore, we applied IF staining to validate the distributed predominance of Macro1 (marked by *CD68*$^+$*SPP1*$^+$) and Macro2 (marked by *CD68*$^+$*MRC1*$^+$) subgroups across three HCC subtypes, finding that the proportional distributions corresponding to their respective subtypes' origin (Fig. 4G). To investigate the impact of *C. sinensis* and HBV double-infection on macrophage polarization, we developed an in vitro co-culture model. Our results revealed that tumor cells treated with CsESPs promoted macrophage polarization toward an M2-like phenotype, as evidenced by elevated expression of CD206 and ARG-1. Furthermore, SPP1 expression was significantly increased in CsESPs-treated HepG2.2.15 cells group (Fig. 4H-J). Taken together, both of scRNA-seq and ST-seq datasets, along with the IF and in vitro examination, uncover the heterogeneity of myeloid cell in HCC subtypes, especially the enrichment of SPP1$^+$ TAMs in DP group.

Identification of the distribution of CD8$^+$ T exhausted cells within the TME

The corpus of existing literature has substantially illuminated the indispensable role of lymphocytes in the etiology, progression, and metastatic cascade of HCC. Our scRNA-seq analysis has delineated fifteen lymphocyte subtypes, encompassing a spectrum of seven CD4$^+$ cell subgroups (CD4_Na, CD4$^+$ T naive cell; CD4_Tm1, CD4$^+$ memory type 1 cell; CD4_Tm2, CD4$^+$ memory type 2 cell, CD4_TF, transcription factor T cell; CD4_Treg, CD4$^+$ regulatory T cell; CD4_Tfh, CD4$^+$ follicular helper T cell, CD4_Cyc, CD4$^+$ cycling cell) and four CD8$^+$ T cell subtypes (CD8_Tem, CD8 effector memory T cell; CD8_Temra, CD8$^+$ recently activated effector memory T cell; CD8_Tex, CD8$^+$ exhausted T cell; CD8_Cyc, CD8$^+$ cycling cell), NK cells, and three B cell subtypes (Bn, B naïve cell; Bm, B memory cell; Plasma, plasma cell) based on cell-specific and canonical marker genes, identified through their distinct and canonical molecular signatures (Fig. 5A-B). Quantitative assessment of cellular proportions discerned congruence between the CP and Normal cohorts, in stark contrast to the divergent profiles observed in the HP and DP groups. This observation underscores the heterogeneity of the immune landscape within the TME of HCC cases. Notably, the HP and DP

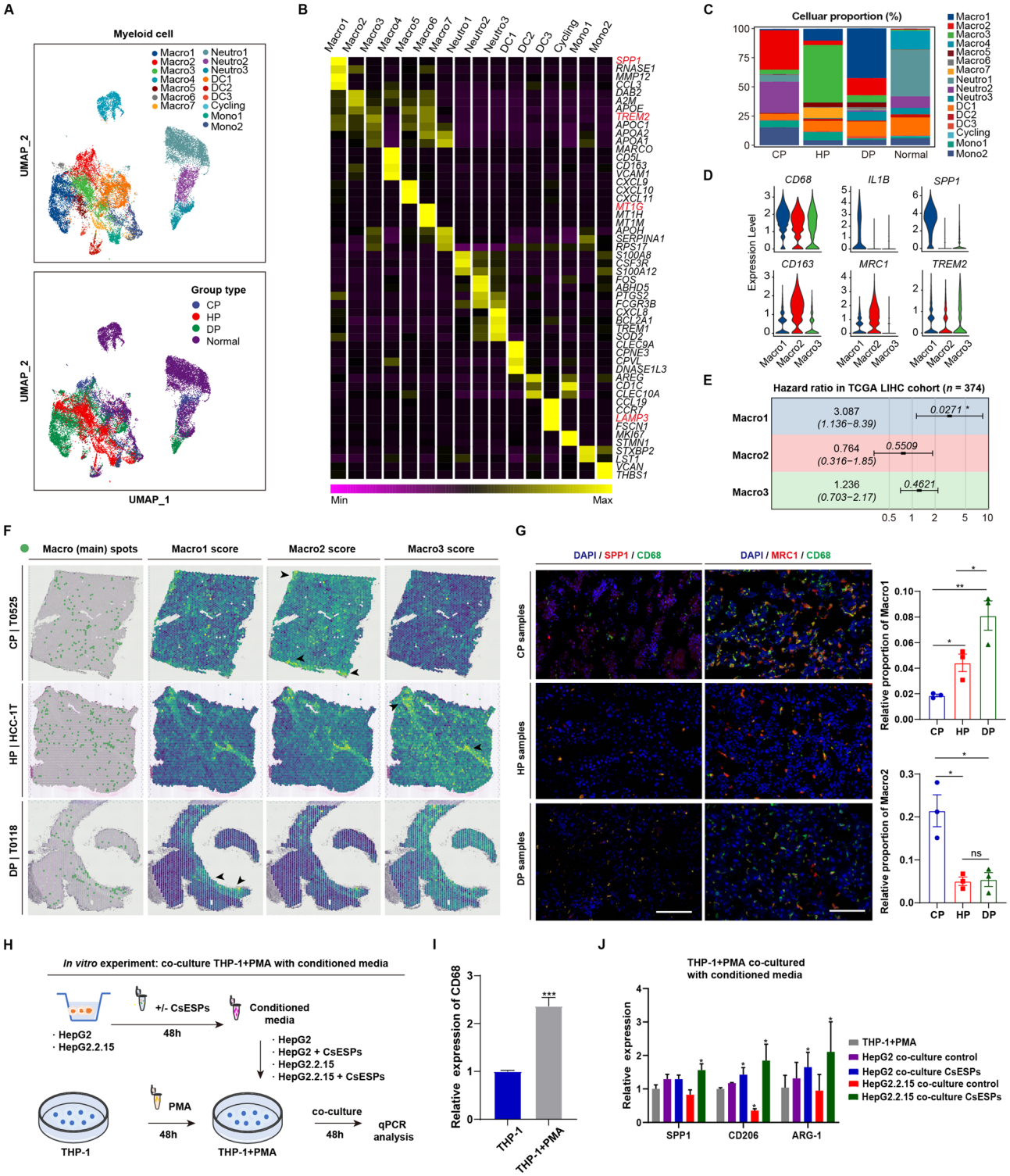

Fig. 4 Figure 4I: The label "Arg-1" has been corrected to "ARG-1".

groups were characterized by an enriched representation of the CD8_Tex and CD4_Treg subtypes (Fig. 5C).

Profiling of gene expression within the CD4_Treg subgroup of the DP group revealed an up-regulation of cytotoxic/effector genes, exemplified by GNLY, and co-inhibitory genes, such as TIGIT, surpassing the levels observed in other cohorts. The DP-derived group also demonstrated heightened expression of co-inhibitory genes, including HAVCR2, LAG3, and BTLA (Fig. S5A). The CD8_Tex subgroup across all HCC cohorts

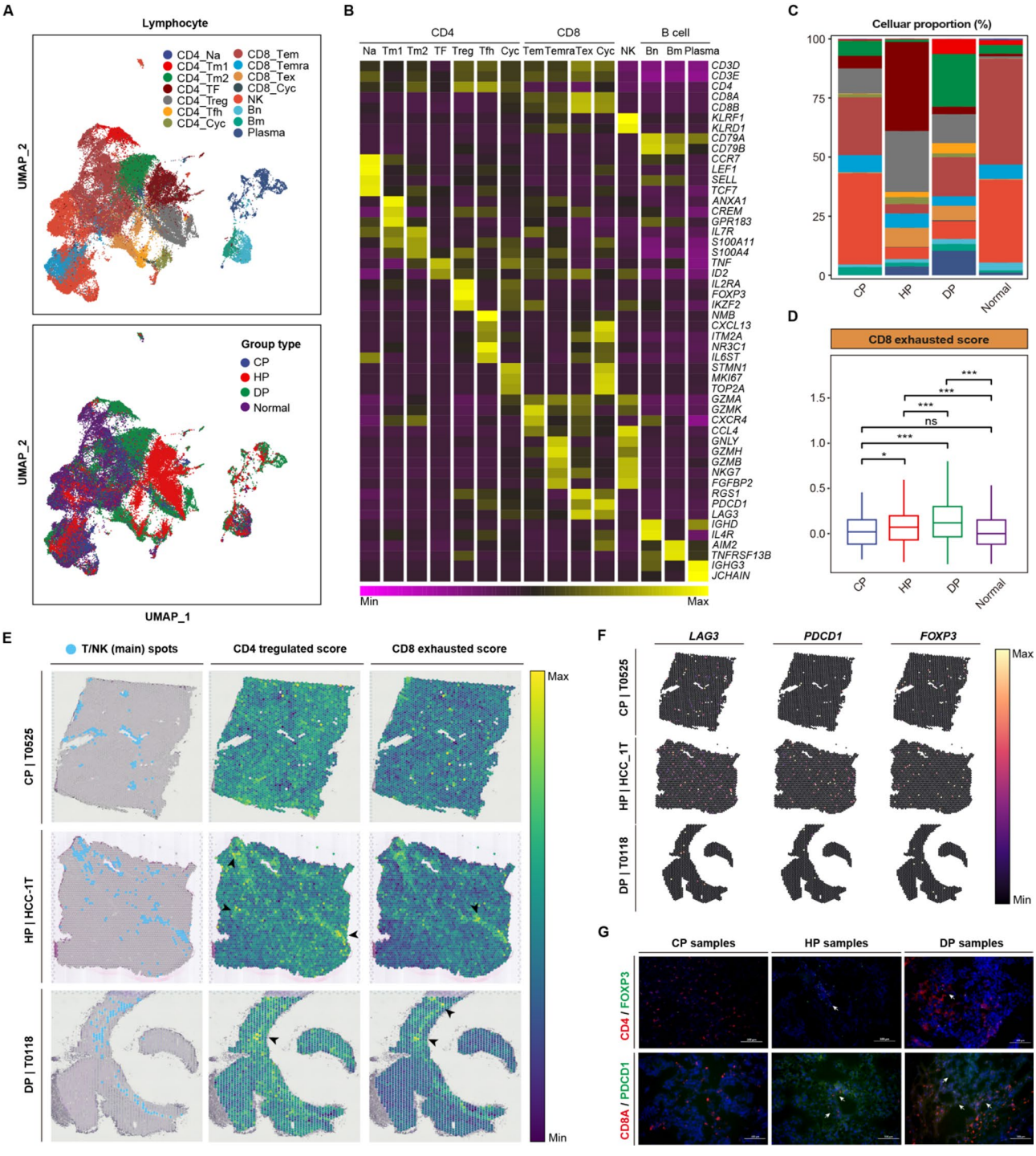

Fig. 5 Characterization of lymphocytes among three HCC groups and normal group. (**A**) The UMAP plots shows the clustering of lymphocytes in the scRNA-seq, colored by lymphocyte subgroups (top panel) and group types (bottom panel). (**B**) The Heatmap shows the expression of cluster-specific markers among T and B cell, and NK subgroups. (**C**) The bar plots show the relative proportion of lymphocytes subgroup among four group types, colored by lymphocyte subgroups. (**D**) The Box plot shows the distribution of CD8 exhausted scores among four groups, *P* values were generated by Wilcoxon rank-sum tests, $^{*}P < 0.05$; $^{***}P < 0.001$; ns, no significant. (**E**) The spatial dimplots show the distribution of lymphocyte spots (highlighted by blue color, left panel), and the distribution of module scores of CD4_Treg and CD8_Tex (middle and right panels) in the ST-seq dataset. (**F**) The spatial feature plots show the expression level of LAG3, PDCD1 and FOXP3 of lymphocyte spots in the HCC sample T0525 (CP), HCC_1T (HP), and T0118 (DP) of the ST-seq dataset. (**G**) The IF staining of CD4_Treg (CD4: red, FOXP3: green) and CD8_Tex (CD8A: red, PDCD1: green) across three HCC subgroups' samples. Scale bar, 100 μm

exhibited significantly elevated scores for tumor-infiltrating CD8 exhaustion compared to the Normal group. Among them, DP group-derived CD8_Tex cells have the highest exhaustion scores within our scRNA-seq dataset (Fig. 5D).

To further elaborate the transcriptomic dynamic of CD8_Tex cells among different groups, we utilized the Monocle algorithm [41] to create a pseudotime trajectory among four group types, creating two separate paths branch1 (indicating cell fate1) and branch2 (indicating cell fate2). According to the pseudotime analysis, we observed CD8_Tex cells from the CP and Normal groups distributed at the beginning part of the trajectory, and DP-derived CD8_Tex cells mainly located in the middle part (cell fate 2), while HP-derived CD8_Tex cells were mainly located in the end segment of trajectory (cell fate 1) (Fig. S5B). After that, we performed BEAM analysis to reveal the transcriptomic alteration of CD8_Tex cell along with the two branches, finding that CD8_Tex in cell fate2 up-regulated immunosuppression-associated signals while CD8_Tex in cell fate1 up-regulated pathways such as regulation of antigen processing and presentation and T cell differentiation (Fig. S5C). Taken together, our results indicated that CD8_Tex cells might exert critical role in reshaping the exhaustive TME in the DP group.

To investigate this at spatial dimension, we also evaluated the CD8 exhausted scores of T/NK spots and found that DP group-derived spots exhibited higher scores than that of the other groups in the ST-seq dataset, in agreement with the result of scRNA-seq analysis (Fig. 5E). We also observed that samples in HP (HCC_1T) and DP (T0118) spatially expressed higher spatial intensity and level of CD8_Tex related markers such as *LAG3*, *PDCD1*, and *FOXP3* (Fig. 5F). Moreover, IF staining substantiated the predominance of CD8A/PDCD1-positive cells within DP group samples (Fig. 5G). These results suggesting that potential cellular infiltration of CD8_Tex contributes to the immunosuppressive TME in both HP and DP groups.

Profiling the inter-tumor microenvironment heterogeneity of stromal cells

The primary stromal cellular components including hepatic stellate cells (HSCs), fibroblasts, and endothelial cells (Endo), are responsible for producing the extracellular components of TME [48, 49]. To investigate the stromal cell composition and their heterogeneity in different HCC types, we re-clustered and annotated stromal cells in the scRNA-seq dataset, forming four Endo subtypes (liver sinusoidal Endo [LSEC, *FCN3*$^+$*CRHBP*$^+$]; liver vascular Endo cluster1 [LVEC_C1, *VWF*$^+$*CLU*$^+$*CXCL12*$^+$], LVEC_C2 [*VWF*$^+$*SPRY1*$^+$*RGCC*$^+$], LVEC_C3 [*ENPP2*$^+$*VWF*$^+$*TTR*$^+$]) and two Fibro subtypes (Fibro_C1 [*FABP4*$^+$*ADIRF*$^+$] and Fibro_C2 [*COL1A2*$^+$*COL3A1*$^+$*COL1A1*$^+$]) (Fig. 6A-B). We further determined the cellular proportion of stromal cell subgroups in the four group types. LSEC cells were predominantly enriched in Normal, while LVEC_C2 were mainly presented in the CP group. LVEC_C3 and Fibro_C2 subtypes were enriched in the HP and DP groups (Fig. 6C).

Ectonucleotide pyrophosphatase-phosphodiesterase 2 (*ENPP2*) has been reported as a novel factor to the pathogenesis of liver fibrosis and cancer [50–52]. By integrating bioinformatic analysis and IHC experiment, we evaluated the expression levels of *ENPP2* among stromal cells, finding that LVEC_C3 subtype from the DP and HP groups exhibits higher expression level of *ENPP2* (Fig. 6D-F). This result was consistent with the elevated expression levels observed in patients during hepatitis C virus infection [53] and increased activity in chronic hepatitis B [54]. Based on DEGs for each subtype, GO enrichment analysis revealed that LVEC_C2 and LVEC_C3 subtypes up-regulated pathways such as extracellular matrix organization, and cell-cell junction organization, while the regulation of cell-matrix adhesion was preferentially up-regulated in Fibro_C2 (Fig. 6G). These findings suggested that the potential cellular interactions between LVEC_C3, Fibro_C2, and other cells within TME of HCC cases.

In the ST-seq datasets, we primarily evaluated the module scores of cell subtypes (LVEC_C3 and Fibro_C2) among stromal spots, finding that HP-derived and DP-derived stromal spots have higher level of Fibro_C2 and LVEC_C3 scores, respectively (Fig. 6H). At spatial dimension, stromal spots exhibit higher module score of LVEC_C3 subtype in the DP group, in contrast to other groups, consistent with the scRNA-seq dataset's finding (Fig. 6I).

Cell-cell interaction relationship among the different groups

As mentioned earlier, our analysis results suggested the potential co-localization and cellular interaction among various cell types such as Macro, T cells and Fibro subtypes. To better understand how HCC affects cell-cell communication within the different HCC groups, we conducted L-R analysis via CellChat to evaluate cellular interaction strength in the scRNA-seq dataset. We initially predicted the interaction numbers within each group, inferring a total of 1,978 L-R pairs mediating interactions. Among these pairs, DP group has the highest interaction count ($n = 605$), while HP group has the lowest count ($n = 300$), indicating that the complicated inter-cellular communication patterns (Fig. 7A). Furthermore, we found the comparison of DP vs. Normal groups contained a stronger interaction strength among key cell subtypes, including Epithelial, CD8_Tex, CD4_Treg, LVEC_C3, Fibro_C2, Macro1, Macro2, and Macro3, compared to other group comparisons (Fig. 7B).

Next, we investigated the critical pathways mediating L-R pairs among these cell subtypes within the four

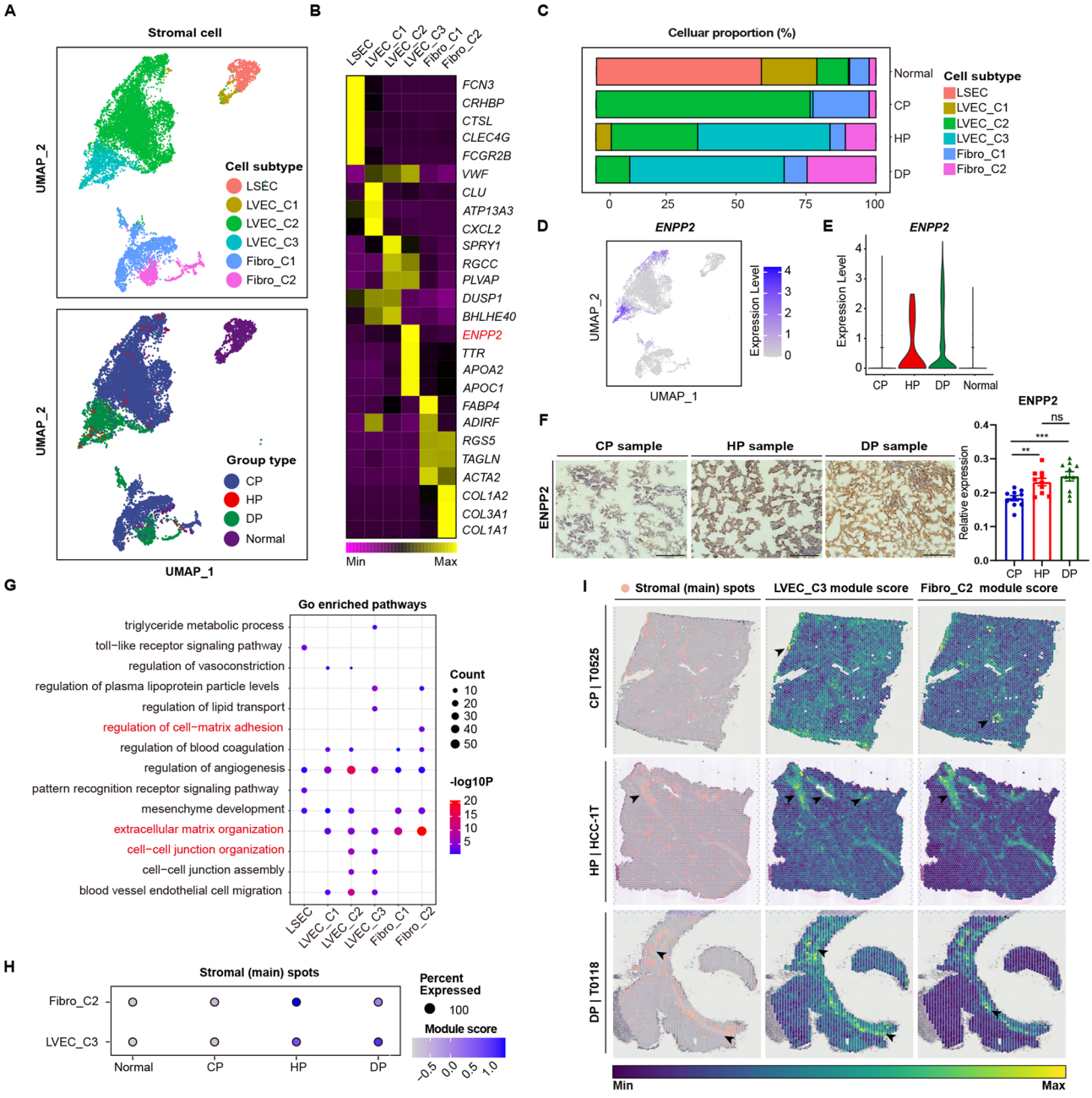

Fig. 6 Characterization of stromal cells among three HCC groups and normal group. (**A**) The UMAP plots shows the clustering of stromal subtype in the scRNA-seq dataset, colored by stromal subgroups (top panel) and group types (bottom panel). (**B**) The heatmap shows the markers expression pattern among stromal cell subtypes. (**C**) The bar plots show the relative proportion of stromal subtype among four group types, colored by subgroup types. (**D**) The feature plot shows the expression level of *ENPP2* in stromal cells in the scRNA-seq dataset. (**E**) The violin plot shows the expression level of *ENPP2* among stromal subtypes in the scRNA-seq dataset. (**F**) Immunohistochemical staining show the expression level of ENPP2 in tumor tissues across three HCC groups (independent cohorts, $n = 3$). Scale bar, 200 μm. (**G**) The bubble plot shows the GO enriched pathways across stromal cell subgroups in the scRNA-seq dataset, the critical pathways were highlight in red. (**H**) The dot plots show the module scores of two stromal subtypes (LVEC_C3 and Fibro_C2) of among stromal spots among four group types in the ST-seq dataset. (**I**) The spatial plots show the distribution of stromal spots (highlighted by pink color, left panel), and the distribution of module scores of LVEC_C3 and Fibro_C2 (middle and right panels) in the ST-seq dataset

groups. Comparing with the Normal group, we identified several overlapping up-regulated differential pathways in three HCC groups, including NECTIN, TIGIT, ANGPT, and PD-L1(Fig. 7C). Of note, we observed up-regulated pathways associated with NOTCH and COLLAGEN in both CP and DP groups (Fig. 7C). The up-regulation of NOTCH pathway in the DP group was consistent with the GSVA results in the Epithelial cell part (Fig. 3E).

After removing the insignificant L-R pairs, we proceeded to determine 6 L-R pairs among these subtypes

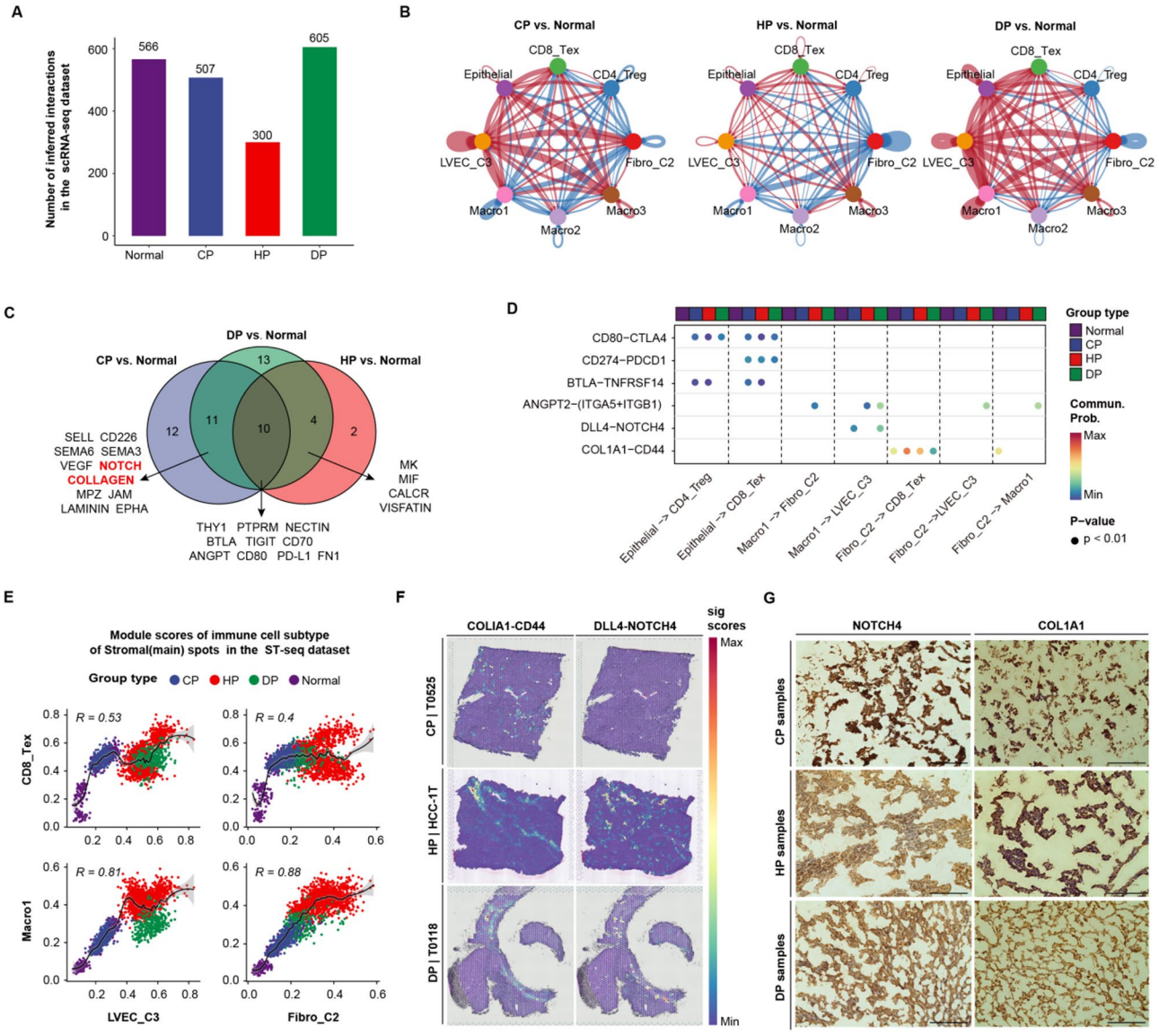

Fig. 7 Intercellular crosstalk analysis of HCC microenvironment. (**A**) Bar plots shows the number of inferred cellular communications' number among four group types. (**B**) Chordal graphs show the differential communication strengthens between CP *vs.* Normal, HP *vs.* Normal, as well as DP *vs.* Normal in the scRNA-seq datasets. (**C**) Venn diagram shows the overlapped differential pathways between CP *vs.* Normal, HP *vs.* Normal as well as DP *vs.* Normal identified in the scRNA-seq dataset. (**D**) Bubble plot shows the interaction probabilities of the significant ligand-receptor (L-R) pairs between sender and receiver cells across four groups of scRNA-seq dataset, colored by group types. (**E**) The scatter plots show the correlation relationship among two immune cell subgroups (CD8_Tex and Macro1) and two stromal subgroups (LVEC_C3 and Fibro_C2) in the stromal spots of ST-seq dataset. (**F**) The ligand-receptor signal scores of DLL4-NOTCH4 pair in the CP (T0525), HP (HCC-1T), and DP (T0118) slides (top panel), The spatial distribution of COL1A1-CD44 ligand-receptor scores in these slides. (**G**) IHC staining show the expression level of NOTCH4 (left panel) and COL1A1 (right panel) in tumor tissues across three HCC groups (independent cohorts, $n = 3$). Scale bar ,200 μm

across different groups (Fig. 7D). Among these interactive pairs, we observed the up-regulation of CD274-PDCD1 pair form Epithelial cell to CD8_Tex, and COL1A1-CD44 pair was significantly up-regulated between Fibro_C2 with CD8_Tex, and Macro1, respectively. Furthermore, we performed correlation analysis between immune module scores (CD8_Tex and Macro1) with the stromal module scores (LVEC_C3 and Fibro_C2) among stromal spots, finding the relative higher correlations coefficient between Macro1with LVEC_C3 ($R = 0.81$) and Fibro_C2 ($R = 0.88$) (Fig. 7E. To further evaluate the key roles of these pathways and L-R pairs, we evaluate DLL4-NOTCH4 and COL1A1-CD44 using the ST-seq slides of three HCC group types via stLearn toolkit (Fig. 7F). Compared with the sample of CP group, we observed the spatially enhanced scores these two L-R pairs in the samples from the HP and DP groups, locating at the cellular distribution of Epithelial and Fibro_C2 groups. We also

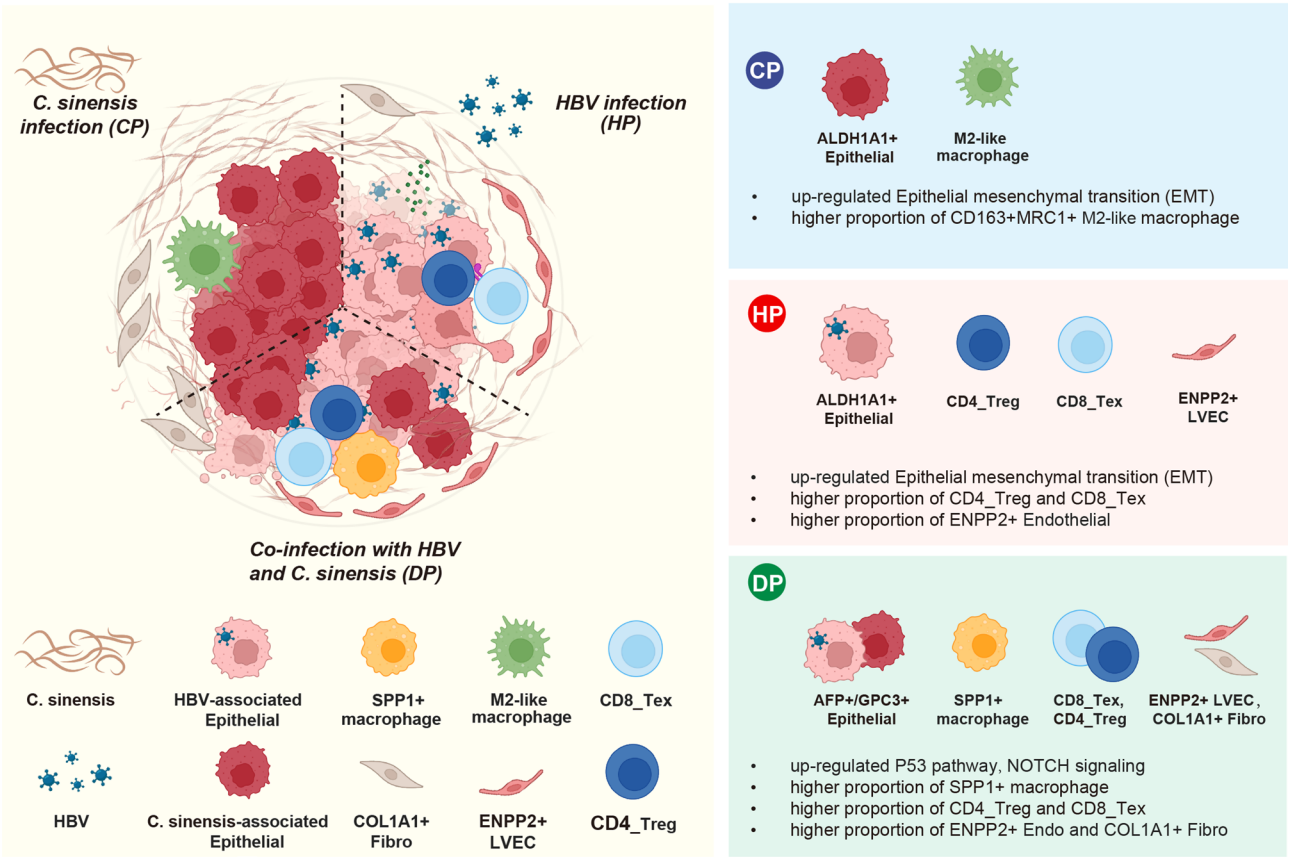

Fig. 8 Summary of inter-tumor heterogeneity and immunosuppressive landscape across different HCC subtypes. *C. Sinensis*, *Clonorchis sinensis*; HBV, Hepatitis B virus; CD8_Tex, $CD8^+$ exhausted T cell; CD4_Treg, $CD4^+$ regulatory T cell; LVEC, liver vascular endothelial cell; Fibro, fibroblast

applied IHC assay to verify the heterogeneous activation of the NOTCH and COLLAGEN pathways among different HCC groups (Fig. 7G). Hence, we profiled the cellular interaction among various cell types that shaping TME of various HCC group types through L-R crosstalk.

Discussion

Here, our study enables characterization of tissue heterogeneity through the identification and spatial visualization of different cell types within single-/double-infected HCC. *C. sinensis* infection has emerged as an imperative carcinogen for HCC in a growing number of Asian countries [11]. Previous researches have provided evidence that *C. sinensis* infection can result in CCA and is associated with a poorer prognosis for HCC [14, 55]. However, the cellular and (or) spatial features of TME of HCC patients with different infected pentagons including HBV and *C. sinensis*, remains to be evaluated. Several studies have investigated the immune microenvironment landscape of HBV-associated HCC [27, 56], but most studies have focused only on HBV-associated HCC (HP), without cross-comparing with *C. sinensis* (CP) or double-infection of *C. sinensis* and HBV-associated HCC (DP). Although the immunosuppressive TME was continuously reported, the potential molecular and cellular mechanisms during the development of HCC cases inflected by distinct pathogens need to be further illustrated. Our multi-omics analysis revealed significant inter-tumor heterogeneity in Epithelial, immune and mesenchymal subgroups across different HCC subtypes. By identifying transcriptional reprograms and and recapitulating the heterogeneous TME occurring in human HCC, we revealed the diverse immune microenvironment in single-/double-infected HCC (Fig. 8).

We primarily evaluated the specific enrichment and features of epithelial cells across different HCC subtypes, finding tumor cells in DP expressing higher levels of *AFP* and *GPC3*. AFP is a diagnostic marker for the detection of HCC. Previous research has reported that AFP was not only strongly associated with malignant characteristics, such as resistance to drug cytotoxicity in HCC, but facilitating the immune escape of HCC [57]. Additionally, the tumor cells in DP shown the high expression levels of cancer stem cell (CSC)-related marker (*CD24*

and *ANPEP*). Liver CSCs were associated with stimulating tumor growth and therapy resistance via shaping an immunosuppressive TME [58]. Moreover, epithelial cells from the DP have higher CNV scores with duplication in chromosomes 9+, 10+, and 22+. Survival analysis based on TCGA database revealed that higher DP tumor cell scores were associated with poor prognosis in HCC patients. We further revealed the distinct patterns of activated hallmark signaling of Epithelial across of each group. We found that epithelial cells from the CP and HP groups exhibited up-regulated pathways of EMT-related signaling, indicating the activation of EMT enhanced the complexity of cellular heterogeneity by altering their plasticity [59, 60]. Notably, epithelial cells in DP group were also marked by the specifically activated pathways of P53, NOTCH, hypoxia, and PI3K-AKT-mTOR, suggesting that these malignant epithelial might be more aggressive compared with other HCC subtypes. Previous studies have shown that upregulation of EMT and P53 signaling pathways promotes metastasis and progression of HCC [61, 62]. A previous study shown that abnormal activity of p53 signaling was identified as causing overexpression of AFP in HCC samples [63], and the transition from epithelial to mesenchymal through the activation of PI3K-Akt/Hypoxia-related signaling strengthened the tumoral angiogenesis and metastasis in HCC [64]. Our results reveal the heterogeneity of Epithelial across different HCC subtypes at marker pattern, genomic alteration, survival state, and activated pathways.

The HCC patients's TME is composed of various immune and stromal cells, such as T lymphocytes [65], TAMs [66], CAFs [67]. The complicate interplay among various cellular and molecular factors shapes the immunosuppressive TME, contributing to the dysfunction and exhaustion of T lymphocytes and immune evasion of tumor cells [23, 68–70]. Interestingly, we found DP-derived cases have an enriched proportion of $SPP1^+$ macrophages (Macro1) expressing pro-inflammatory factors (*CD68* and *IL1B*). It was reported that $SPP1^+$ macrophage was defined as a novel biomarker for the tumor-promoting macrophage derived by monocytes, which was associated with immunosuppression via interacting with T lymphocytes [71]. A recent study on HCC indicated the co-location of $SPP1^+$ macrophages and tumor cell exacerbate the hypoxia TME [72]. $SPP1^+$ macrophages played a role in preventing T cells from infiltrating the tumor region and were linked to a poorer prognosis [73], consistent with the higher hazard ratio of $SPP1^+$ macrophages in patients. Therefore, specifically targeting $SPP1^+$ macrophages have the potential to reduce their immunosuppressive capabilities and promote T cell function, so as to improve the therapeutic effects for DP subgroups.

As for the lymphocytes, our multi-omics dataset revealed a different composition of T lymphocyte across different groups, finding the prevalence of CD4_Treg and CD8_Tex in both HP and DP groups compared with those from other two groups. CD8_Tex exhibits diminished effector function and increased expression levels of inhibitory factors (PD-1/TIGIT), which significantly limits the anti-tumor immune response of $CD8^+$ T cells [74, 75]. Notably, both of dataset and experiment indicated the enrichment of CD8_Tex subgroup in the DP samples, with higher CD8 exhausted score across HCC subtypes. Pseudotime analysis further demonstrated that CD8_Tex cells were primarily differentiated as two branches based on their group-derived origins, represented by different enriched pathways. For example, GO analysis revealed the negative regulatory of immune process of CD8_Tex cells in the DP group, suggesting that patients in the DP group were characterized an immunosuppressive TME than other HCC subtypes, and these patients might have potential benefit upon immunotherapy in targeting CD8_Tex cells.

Multiple studies suggested the rapidly proliferating tumor cells and sophisticated cellular interaction commonly shape the immunosuppressive TME [76–79]. In cellular crosstalk analysis, both of scRNA-seq and ST-seq results revealed the high possibility of cellular interaction between Fibro_C2 and CD8_Tex via COL1A1-CD44 L-R pair, and Macro1 and LVEC_C3 via DLL4-NOTCH4 L-R pair, suggesting that these cellular interactions contribute to the formation of immunosuppressive TME. These key L-R pairs also help shape TME heterogeneity among CP, HP and DP. COL1A1, as a key component of extracellular matrix, contributes to various biological processes, including cell migration, angiogenesis, and matrix remodeling and tumor adhesion [80–82]. These processes are largely mediated through ECM-associated receptors such as CD44, and integrins [83]. Additionally, DLL4-NOTCH signaling nurtures the self-renewal of cancer stem-like cells [84]. It also interacts with signaling pathways such as PI3K, EGFR, and MMP-9, which are closely linked to tumor invasion, proliferation, and metastasis [85, 86].

Our findings provided comprehensive insights into molecular and pathological properties that imparted ecosystem differences in HCC subtypes, and could be possible targets of immunotherapy for single-/double-infected HCC patients. On one hand, the molecular typing-guided precision intervention is recommended for the characteristic signaling pathway abnormalities of epithelial cells in HCC of different infection types. For patients in the DP group with activation of the p53 signaling pathway, p53's function restoration therapy can be prioritized; while patients in the CP/HP groups are suitable for therapeutic strategies targeting the EMT process to inhibit tumor metastasis. On the other hand, the $SPP1^+$ macrophage enrichment phenomenon characteristic of the DP group

suggests that the tumor microenvironment of this subtype is characterized by significant immunosuppression. The combined application of macrophage reprogramming strategies with PD-1/PD-L1 inhibitors was suggested to potentially enhance immunotherapy response by reversing the immunosuppressive microenvironment. Notably, the prevalence of CD8_Tex cells in HCC groups provides a theoretical basis for the application of immune checkpoint inhibitors. In particular, the combination regimen of PD-1 inhibitors combined with TIM-3 inhibitors or LAG-3 inhibitors is recommended for DP patients, which is expected to significantly enhance therapeutic efficacy through multi-targeted blockade of T-cell inhibitory signaling.

This study has several limitations. Firstly, a major technical limitation of our ST-seq dataset is the lack of single-cell resolution, with each spot capturing transcripts from 10 to 200 cells according to tissue types [87, 88]. The challenge might complicate the incorporation of current approaches with cell-cell interactions at spatial dimension [88]. Secondly, our study mainly revealed the characteristics of the TME of HCC cases with different infection types, but we didn't enroll patients underwent treatment to further evaluate the heterogeneity in response to clinical therapy. Thirdly, the findings about feature or biomarkers in our study, such as the predominant cellular subgroup, activated pathways, is warrant further validation in HCC cohort with larger number of clinical cases of different HCC subtypes. Finally, we here conducted integrated analysis to profile the divergence of transcriptomic pattern of the composition within the HCC TME, while the heterogeneity of these elements in genomics, proteomics, and epigenomics of different HCC subtypes, were still need to be further explored.

In summary, we comprehensively analyzed the cellular features, spatial landscapes, and intercellular interactions of different HCC cases infected with HBV and *C. sinensis*. By comparing three different infection types of HCC, we identified the heterogeneity of the tumor microenvironment, transcriptomics diversity, and tumor-associated pathway activity of different HCC subtypes, as well as the patterns of cellular interactions within the TME. These findings not only deepen the understanding of the heterogeneous multicellular ecosystem in different infection types of HCC, but also provide an important reference for the establishment of a precise treatment system based on molecular typing.

Supplementary Information

The online version contains supplementary material available at https://doi.org/10.1186/s12943-025-02381-z.

Supplementary Material 1

Supplementary Material 2

Supplementary Material 3

Supplementary Material 4

Supplementary Material 5

Acknowledgements
None.

Author contributions
JG. W and GD. L designed the experiments and supervised the project. XW. L, GZ. Z, J. F, JQ. L, WM. L and ZJ. L planned and collected the clinical samples. T. P, provided HCC cohort data. JY. C, J. L and YM. B performed data analysis and interpretation. JY. C, WM. L, YN. L, and J. L drafted the manuscript. WM. L and ZJ. L performed the experiments. J. Z provided essential suggestions regarding experiments. JG. W, LQ. J, and GD. L reviewed the manuscript. All authors approved the final version of the paper.

Funding
We gratefully acknowledge the financial support from the National Key Research and Development Program of China (No.2022YFC2303603); the Scientific and technological innovation project of China Academy of Chinese Medical Sciences (CI2023D003, CI2023E005TS05); the National Natural Science Foundation of China (82572600, 82560579, 82074098, 82274182, 82441001); the CACMS Innovation Fund (CI2023E002, ZG2024001-05, CI2021A05101); the Establishment of Sino-Austria "Belt and Road" Joint Laboratory on Traditional Chinese Medicine for Severe Infectious Diseases and Joint Research (2020YFE0205100); the Science and Technology Foundation of Shenzhen (Shenzhen Clinical Medical Research Center for Geriatric Diseases); the Shenzhen Medical Research Funds (B2302051); the Distinguished Expert Project of Sichuan Province Tianfu Scholar (CW202002); the Fundamental Research Funds for the Central Public Welfare Research Institutes (ZZ18-ND-10, ZZ17-ND-10, ZZ16-ND-10-23, ZZ15-ND-10, ZZ14-ND-010, ZZ14-FL-010, ZZ14-YQ-050, ZZ13-ZD-07); the Natural Science Foundation of Shanghai (24ZR1414000), Guangxi Natural Science Foundation (2024GXNSFDA010029, 2025GXNSFAA069704), the Key Laboratory of Early Prevention and Treatment for Regional High Frequency Tumor (Guangxi Medical University), Ministry of Education (GKE-ZZ202131), and the Innovation Project of Guangxi Graduate Education (YCBZ2024142). All authors gave approval of the final version for publication.

Data availability
The raw single-cell and spatial transcriptome sequencing datasets are deposited in the Genome Sequence Archive (GSA for human) (https://bigd.big.ac.cn/gsa/,accession number HRA008527 and HRA008666, respectively).

Declarations

Ethics approval and consent to participate
This study was centrally approved by the Ethical committee of the First Affiliated Hospital of Guangxi Medical University (No. 2024-E580-01) and complied with all relevant ethical requirements. The patients provided written informed consent to participate in this study. The authors are accountable for all aspects of the work and for ensuring that the accuracy or integrity of any part of the work are appropriately investigated and resolved.

Consent for publication
Not applicable.

Competing interests
The authors declare no competing interests.

Author details
[1]Department of Toxicology, School of Public Health, Guangxi Medical University, Nanning, Guangxi 530021, China
[2]State Key Laboratory for Quality Ensurance and Sustainable Use of Dao-di Herbs, Artemisinin Research Center, Institute of Chinese Materia Medica, China Academy of Chinese Medical Sciences, Beijing 100700, China

[3]Center for Drug Research and Development, Guangdong Provincial Key Laboratory for Research and Evaluation of Pharmaceutical Preparations, Guangdong Pharmaceutical University, Guangzhou, Guangdong 510006, China
[4]Department of Integrative Oncology, China-Japan Friendship Hospital, No. 2 East Yinghua Road, Chaoyang District, Beijing 100029, China
[5]Department of Hepatobiliary Surgery, The First Affiliated Hospital of Guangxi Medical University, 6 Shuangyong Road, Nanning, Guangxi 530021, China
[6]School of Public Health, Fudan University, 130 Dong-An Road, Shanghai 200032, China
[7]Department of Physiology, School of Preclinical Medicine, Guangxi Medical University, 22 Shuangyong Road, Nanning, Guangxi 530021, China

Received: 12 March 2025 / Accepted: 6 June 2025
Published online: 05 January 2026

References

1. Sung H, Ferlay J, Siegel RL, et al. Global Cancer statistics 2020: GLOBOCAN estimates of incidence and mortality worldwide for 36 cancers in 185 countries. CA Cancer J Clin. 2021;71(3):209–49.
2. Bray F, Laversanne M, Sung H, et al. Global cancer statistics 2022: GLOBOCAN estimates of incidence and mortality worldwide for 36 cancers in 185 countries. CA Cancer J Clin. 2024;74(3):229–63.
3. Bray F, Ferlay J, Soerjomataram I, et al. Global cancer statistics 2018: GLOBOCAN estimates of incidence and mortality worldwide for 36 cancers in 185 countries. CA Cancer J Clin. 2018;68(6):394–424.
4. Siegel RL, Miller KD, Fuchs HE, et al. Cancer statistics, 2022. CA Cancer J Clin. 2022;72(1):7–33.
5. Singal AG, Kanwal F, Llovet JM. Global trends in hepatocellular carcinoma epidemiology: implications for screening, prevention and therapy. Nat Rev Clin Oncol. 2023;20(12):864–84.
6. Jia L, Gao Y, He Y, et al. HBV induced hepatocellular carcinoma and related potential immunotherapy. Pharmacol Res. 2020;159:104992.
7. Devarbhavi H, Asrani SK, Arab JP, et al. Global burden of liver disease: 2023 update. J Hepatol. 2023;79(2):516–37.
8. Tang ZL, Huang Y, Yu XB. Current status and perspectives of Clonorchis sinensis and clonorchiasis: epidemiology, pathogenesis, omics, prevention and control. Infect Dis Poverty. 2016;5(1):71.
9. Qian MB, Utzinger J, Keiser J, et al. Clonorchiasis Lancet. 2016;387(10020):800–10.
10. Bouvard V, Baan R, Straif K, et al. A review of human carcinogens–Part B: biological agents. Lancet Oncol. 2009;10(4):321–2.
11. Shi Y, Jiang Z, Yang Y, et al. Clonorchis sinensis infection and co-infection with the hepatitis B virus are important factors associated with cholangiocarcinoma and hepatocellular carcinoma. Parasitol Res. 2017;116(10):2645–9.
12. Qi Y, Hu J, Liang J, et al. Clonorchis sinensis infection contributes to hepatocellular carcinoma progression in rat. Parasitol Res. 2022;121(12):3403–15.
13. Wang C, He Q, Yin Y, et al. Clonorchis sinensis granulin promotes malignant transformation of hepatocyte through EGFR-Mediated RAS/MAPK/ERK and PI3K/Akt signaling pathways. Front Cell Infect Microbiol. 2021;11:734750.
14. Li YK, Zhao JF, Yang CL, et al. Effects of Clonorchis sinensis combined with hepatitis B virus infection on the prognosis of patients with hepatocellular carcinoma following hepatectomy. PLoS Negl Trop Dis. 2023;17(1):e0011012.
15. Balkwill FR, Capasso M, Hagemann T. The tumor microenvironment at a glance. J Cell Sci. 2012;125(Pt 23):5591–6.
16. de Visser KE, Joyce JA. The evolving tumor microenvironment: from cancer initiation to metastatic outgrowth. Cancer Cell. 2023;41(3):374–403.
17. Binnewies M, Roberts EW, Kersten K, et al. Understanding the tumor immune microenvironment (TIME) for effective therapy. Nat Med. 2018;24(5):541–50.
18. Liu Y, Xun Z, Ma K, et al. Identification of a tumour immune barrier in the HCC microenvironment that determines the efficacy of immunotherapy. J Hepatol. 2023;78(4):770–82.
19. Sun Y, Wu L, Zhong Y, et al. Single-cell landscape of the ecosystem in early-relapse hepatocellular carcinoma. Cell. 2021;184(2):404–21. e416.
20. Chen S, Huang C, Liao G, et al. Distinct single-cell immune ecosystems distinguish true and de Novo HBV-related hepatocellular carcinoma recurrences. Gut. 2023;72(6):1196–210.
21. Xue R, Zhang Q, Cao Q, et al. Liver tumour immune microenvironment subtypes and neutrophil heterogeneity. Nature. 2022;612(7938):141–7.
22. Zheng C, Zheng L, Yoo JK, et al. Landscape of infiltrating T cells in liver Cancer revealed by Single-Cell sequencing. Cell. 2017;169(7):1342–56. e1316.
23. Zhang Q, He Y, Luo N, et al. Landscape and dynamics of single immune cells in hepatocellular carcinoma. Cell. 2019;179(4):829–e845820.
24. Wu R, Guo W, Qiu X, et al. Comprehensive analysis of Spatial architecture in primary liver cancer. Sci Adv. 2021;7(51):eabg3750.
25. Wu Y, Yang S, Ma J, et al. Spatiotemporal immune landscape of colorectal Cancer liver metastasis at Single-Cell level. Cancer Discov. 2022;12(1):134–53.
26. Tian B, Li Q. Single-Cell sequencing and its applications in liver Cancer. Front Oncol. 2022;12:857037.
27. Ho DW, Tsui YM, Chan LK, et al. Single-cell RNA sequencing shows the immunosuppressive landscape and tumor heterogeneity of HBV-associated hepatocellular carcinoma. Nat Commun. 2021;12(1):3684.
28. Lu Y, Yang A, Quan C, et al. A single-cell atlas of the multicellular ecosystem of primary and metastatic hepatocellular carcinoma. Nat Commun. 2022;13(1):4594.
29. Zhou J, Sun H, Wang Z, et al. Guidelines for the diagnosis and treatment of primary liver Cancer (2022 Edition). Liver Cancer. 2023;12(5):405–44.
30. Ying-Dan C, Ting-Jun Z, Long-Qi X, et al. [Interpretation of diagnostic criteria for clonorchiasis]. Zhongguo Xue Xi Chong Bing Fang Zhi Za Zhi. 2017;29(5):538–40.
31. Hepatitis B. Virus infection. Nat Rev Dis Primers. 2018;4:18036.
32. Satija R, Farrell JA, Gennert D, et al. Spatial reconstruction of single-cell gene expression data. Nat Biotechnol. 2015;33(5):495–502.
33. Korsunsky I, Millard N, Fan J, et al. Fast, sensitive and accurate integration of single-cell data with harmony. Nat Methods. 2019;16(12):1289–96.
34. Liu J, Shi Y, Zhang Y. Multi-omics identification of an Immunogenic cell death-related signature for clear cell renal cell carcinoma in the context of 3P medicine and based on a 101-combination machine learning computational framework. EPMA J. 2023;14(2):275–305.
35. Moncada R, Barkley D, Wagner F, et al. Integrating microarray-based Spatial transcriptomics and single-cell RNA-seq reveals tissue architecture in pancreatic ductal adenocarcinomas. Nat Biotechnol. 2020;38(3):333–42.
36. Wu T, Hu E, Xu S, et al. ClusterProfiler 4.0: A universal enrichment tool for interpreting omics data. Innov (Camb). 2021;2(3):100141.
37. Hanzelmann S, Castelo R, Guinney J. GSVA: gene set variation analysis for microarray and RNA-seq data. BMC Bioinformatics. 2013;14:7.
38. Liberzon A, Birger C, Thorvaldsdottir H, et al. The molecular signatures database (MSigDB) hallmark gene set collection. Cell Syst. 2015;1(6):417–25.
39. Venteicher AS, Tirosh I, Hebert C, et al. Decoupling genetics, lineages, and microenvironment in IDH-mutant gliomas by single-cell RNA-seq. Science. 2017;355:6332.
40. Puram SV, Tirosh I, Parikh AS, et al. Single-Cell transcriptomic analysis of primary and metastatic tumor ecosystems in head and neck Cancer. Cell. 2017;171(7):1611–e16241624.
41. Qiu X, Hill A, Packer J, et al. Single-cell mRNA quantification and differential analysis with census. Nat Methods. 2017;14(3):309–15.
42. Ji AL, Rubin AJ, Thrane K, et al. Multimodal analysis of composition and Spatial architecture in human squamous cell carcinoma. Cell. 2020;182(6):1661–2.
43. Jin S, Guerrero-Juarez CF, Zhang L, et al. Inference and analysis of cell-cell communication using cellchat. Nat Commun. 2021;12(1):1088.
44. Chung W, Eum HH, Lee HO, et al. Single-cell RNA-seq enables comprehensive tumour and immune cell profiling in primary breast cancer. Nat Commun. 2017;8:15081.
45. Xing X, Yang F, Huang Q et al. Decoding the multicellular ecosystem of lung adenocarcinoma manifested as pulmonary subsolid nodules by single-cell RNA sequencing. Sci Adv. 2021;7(5).
46. Yi K, Wang Y, Rong Y, et al. Transcriptomic signature of 3D hierarchical porous chip enriched exosomes for early detection and progression monitoring of hepatocellular carcinoma. Adv Sci (Weinh). 2024;11(14):e2305204.
47. Tojjari A, Hafez AH, Saeed A, et al. Exploring Glypican-3 as a molecular target in hepatocellular carcinoma: perspectives on diagnosis and precision immunotherapy strategies. Front Biosci (Landmark Ed). 2024;29(7):268.
48. Novikova MV, Khromova NV, Kopnin PB. Components of the hepatocellular carcinoma microenvironment and their role in tumor progression. Biochem (Mosc). 2017;82(8):861–73.
49. Dhar D, Baglieri J, Kisseleva T, et al. Mechanisms of liver fibrosis and its role in liver cancer. Exp Biol Med (Maywood). 2020;245(2):96–108.
50. Meng J, Ruan X, Wei F, et al. High expression of ENPP2 is an independent predictor of poor prognosis in liver cancer. Med (Baltim). 2023;102(31):e34480.

51. Nishimasu H, Ishitani R, Aoki J, et al. A 3D view of autotaxin. Trends Pharmacol Sci. 2012;33(3):138–45.
52. Kaffe E, Katsifa A, Xylourgidis N, et al. Hepatocyte autotaxin expression promotes liver fibrosis and cancer. Hepatology. 2017;65(4):1369–83.
53. Kostadinova L, Shive CL, Judge C, et al. During hepatitis C virus (HCV) infection and HCV-HIV coinfection, an elevated plasma level of autotaxin is associated with lysophosphatidic acid and markers of immune activation that normalize during Interferon-Free HCV therapy. J Infect Dis. 2016;214(9):1438–48.
54. Joshita S, Ichikawa Y, Umemura T, et al. Serum autotaxin is a useful liver fibrosis marker in patients with chronic hepatitis B virus infection. Hepatol Res. 2018;48(4):275–85.
55. Xu L, Zhang Y, Lin Z, et al. FASN-mediated fatty acid biosynthesis remodels immune environment in Clonorchis sinensis infection-related intrahepatic cholangiocarcinoma. J Hepatol. 2024;81(2):265–77.
56. Lim CJ, Lee YH, Pan L, et al. Multidimensional analyses reveal distinct immune microenvironment in hepatitis B virus-related hepatocellular carcinoma. Gut. 2019;68(5):916–27.
57. Li M, Liu X, Zhou S, et al. Effects of alpha Fetoprotein on escape of Bel 7402 cells from attack of lymphocytes. BMC Cancer. 2005;5:96.
58. Tsui YM, Chan LK, Ng IO. Cancer stemness in hepatocellular carcinoma: mechanisms and translational potential. Br J Cancer. 2020;122(10):1428–40.
59. Yoon SM, Gerasimidou D, Kuwahara R, et al. Epithelial cell adhesion molecule (EpCAM) marks hepatocytes newly derived from stem/progenitor cells in humans. Hepatology. 2011;53(3):964–73.
60. Giannelli G, Koudelkova P, Dituri F, et al. Role of epithelial to mesenchymal transition in hepatocellular carcinoma. J Hepatol. 2016;65(4):798–808.
61. Alqurashi YE, Al-Hetty H, Ramaiah P, et al. Harnessing function of EMT in hepatocellular carcinoma: from biological view to Nanotechnological standpoint. Environ Res. 2023;227:115683.
62. Makino Y, Hikita H, Fukumoto K, et al. Constitutive activation of the tumor suppressor p53 in hepatocytes paradoxically promotes Non-Cell autonomous liver carcinogenesis. Cancer Res. 2022;82(16):2860–73.
63. Peng SY, Chen WJ, Lai PL, et al. High alpha-fetoprotein level correlates with high stage, early recurrence and poor prognosis of hepatocellular carcinoma: significance of hepatitis virus infection, age, p53 and beta-catenin mutations. Int J Cancer. 2004;112(1):44–50.
64. Fu J, Chen Y, Cao J, et al. p28GANK overexpression accelerates hepatocellular carcinoma invasiveness and metastasis via phosphoinositol 3-kinase/AKT/hypoxia-inducible factor-1alpha pathways. Hepatology. 2011;53(1):181–92.
65. Gupta T, Jarpula NS. Hepatocellular carcinoma immune microenvironment and check point inhibitors-current status. World J Hepatol. 2024;16(3):353–65.
66. Li Z, Duan D, Li L, et al. Tumor-associated macrophages in anti-PD-1/PD-L1 immunotherapy for hepatocellular carcinoma: recent research progress. Front Pharmacol. 2024;15:1382256.
67. Chen Y, McAndrews KM, Kalluri R. Clinical and therapeutic relevance of cancer-associated fibroblasts. Nat Rev Clin Oncol. 2021;18(12):792–804.
68. Aizarani N, Saviano A, Sagar, et al. A human liver cell atlas reveals heterogeneity and epithelial progenitors. Nature. 2019;572(7768):199–204.
69. Sharma A, Seow JJW, Dutertre CA, et al. Onco-fetal reprogramming of endothelial cells drives immunosuppressive macrophages in hepatocellular carcinoma. Cell. 2020;183(2):377–94. e321.
70. Song G, Shi Y, Zhang M, et al. Global immune characterization of HBV/HCV-related hepatocellular carcinoma identifies macrophage and T-cell subsets associated with disease progression. Cell Discov. 2020;6(1):90.
71. Matsubara E, Komohara Y, Esumi S et al. SPP1 derived from macrophages is associated with a worse clinical course and Chemo-Resistance in lung adenocarcinoma. Cancers (Basel). 2022;14(18).
72. Fan G, Xie T, Li L, et al. Single-cell and Spatial analyses revealed the co-location of cancer stem cells and SPP1 + macrophage in hypoxic region that determines the poor prognosis in hepatocellular carcinoma. NPJ Precis Oncol. 2024;8(1):75.
73. Cess CG, Finley SD. Multi-scale modeling of macrophage-T cell interactions within the tumor microenvironment. PLoS Comput Biol. 2020;16(12):e1008519.
74. Tang T, Huang X, Zhang G, et al. Advantages of targeting the tumor immune microenvironment over blocking immune checkpoint in cancer immunotherapy. Signal Transduct Target Ther. 2021;6(1):72.
75. Kraehenbuehl L, Weng CH, Eghbali S, et al. Enhancing immunotherapy in cancer by targeting emerging Immunomodulatory pathways. Nat Rev Clin Oncol. 2022;19(1):37–50.
76. Hanahan D, Weinberg RA. Hallmarks of cancer: the next generation. Cell. 2011;144(5):646–74.
77. Jain RK. Normalizing tumor microenvironment to treat cancer: bench to bedside to biomarkers. J Clin Oncol. 2013;31(17):2205–18.
78. Jain RK. Antiangiogenesis strategies revisited: from starving tumors to alleviating hypoxia. Cancer Cell. 2014;26(5):605–22.
79. Li SQ, Yang Y, Ye LS. Angiogenesis and immune checkpoint dual blockade: opportunities and challenges for hepatocellular carcinoma therapy. World J Gastroenterol. 2022;28(42):6034–44.
80. Yang MC, Wang CJ, Liao PC, et al. Hepatic stellate cells secretes type I collagen to trigger epithelial mesenchymal transition of hepatoma cells. Am J Cancer Res. 2014;4(6):751–63.
81. Gilkes DM, Semenza GL, Wirtz D. Hypoxia and the extracellular matrix: drivers of tumour metastasis. Nat Rev Cancer. 2014;14(6):430–9.
82. Bonnans C, Chou J, Werb Z. Remodelling the extracellular matrix in development and disease. Nat Rev Mol Cell Biol. 2014;15(12):786–801.
83. Multhaupt HA, Leitinger B, Gullberg D, et al. Extracellular matrix component signaling in cancer. Adv Drug Deliv Rev. 2016;97:28–40.
84. Zhu TS, Costello MA, Talsma CE, et al. Endothelial cells create a stem cell niche in glioblastoma by providing NOTCH ligands that nurture self-renewal of cancer stem-like cells. Cancer Res. 2011;71(18):6061–72.
85. Kenig S, Alonso MB, Mueller MM, et al. Glioblastoma and endothelial cells cross-talk, mediated by SDF-1, enhances tumour invasion and endothelial proliferation by increasing expression of cathepsins B, S, and MMP-9. Cancer Lett. 2010;289(1):53–61.
86. Cheng L, Huang Z, Zhou W, et al. Glioblastoma stem cells generate vascular pericytes to support vessel function and tumor growth. Cell. 2013;153(1):139–52.
87. Saiselet M, Rodrigues-Vitoria J, Tourneur A, et al. Transcriptional output, cell-type densities, and normalization in Spatial transcriptomics. J Mol Cell Biol. 2020;12(11):906–8.
88. Cang Z, Nie Q. Inferring Spatial and signaling relationships between cells from single cell transcriptomic data. Nat Commun. 2020;11(1):2084.

Publisher's note